An ANSYS user cohesive element for the modelling of fatigue initiation and propagation of delaminations in composite structures

Urcelay Oca, Inigo; Bak, Brian Lau Verndal; Turon, Albert; Lindgaard, Esben

Published in:
Engineering Fracture Mechanics

DOI (link to publication from Publisher):
10.1016/j.engfracmech.2024.110337

Publication date:
2024

Document Version
Publisher's PDF, also known as Version of record

Engineering Fracture Mechanics 308 (2024) 110337

Contents lists available at ScienceDirect

Engineering Fracture Mechanics

journal homepage: www.elsevier.com/locate/engfracmech

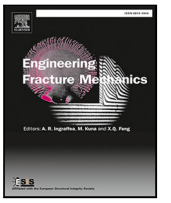

An ANSYS user cohesive element for the modelling of fatigue initiation and propagation of delaminations in composite structures

Iñigo Urcelay Oca [a,b], Brian Lau Verndal Bak [b], Albert Turon [c], Esben Lindgaard [b,*]

[a] Siemens Gamesa Renewable Energy, Assensvej 11, Aalborg, 9220, Denmark
[b] CraCS Research Group, Department of Materials and Production, Aalborg University, Fibigerstraede 16, Aalborg, 9220, Denmark[1]
[c] Analysis and Advanced Materials for Structural Design (AMADE), Polytechnic School, University of Girona, Campus Montilivi s/n, Girona, 17003, Spain

ARTICLE INFO

Dataset link: https://github.com/CraCS-research-group/ANSYS-Fatigue-Cohesive-Element

Keywords:
Composite materials
Delamination
Fatigue propagation
Fatigue initiation
Cohesive element

ABSTRACT

A deeper understanding of delamination growth under fatigue loading in composite wind turbine blades is required. A new cohesive model for delamination fatigue initiation, which uses initiation S-N curve data to calculate the number of cycles to the introduction of delaminations, is developed and tailored to a state-of-the-art model for fatigue propagation. Both models are implemented in a novel user-defined cohesive element for ANSYS Mechanical APDL. In fatigue propagation-dominated test cases, including with multiple delaminations, the crack growth rate evolution is accurately predicted. In fatigue initiation-dominated cases, a satisfactory prediction is achieved, also showcasing the ability to model fatigue propagation after initiation.

1. Introduction

Wind energy plays a vital role towards the decarbonisation of energy production. One prominent trend in the wind industry is the manufacturing of increasingly large blades to expand the energy harvesting capability per rotor. Another major trend is the search for solutions that reduce the waste generated by wind turbines at the end of their service life by, for example, extending such service life to maximise their potential further. There is, thus, an overall aim for longer blades in service for an increasing number of years. To achieve this aim, it becomes increasingly necessary to understand better how damage initiates and propagates under fatigue loading. One damage type specifically relevant in composite structures is delaminations, where the crack propagates in the interface between the composite plies in a laminate.

Cohesive elements are widely used in finite element analyses for modelling the initiation and propagation of delaminations in composite structures. Numerous researchers have employed cohesive elements to study the effect of delaminations in wind turbine blades. This approach has been used to model the monotonous loading and subsequent failure of pristine blades [1–3] and sub-components representative of specific design details [4,5]. Cohesive elements have also been used to study the effect of manufacturing defects, such as delaminations themselves [6] or those initiated by wrinkles [7–11]. Nevertheless, most of the previous work was restricted to delaminations under static loading, even if blade design is generally fatigue-driven.

Various researchers have proposed different approaches for modelling delamination propagation and initiation under fatigue loading with cohesive elements. Initiation refers to the generation of a delamination in pristine laminates.

* Corresponding author.
E-mail addresses: inigo.oca@siemensgamesa.com (I.U. Oca), brianbak@mp.aau.dk (B.L.V. Bak), albert.turon@udg.edu (A. Turon), elo@mp.aau.dk (E. Lindgaard).
[1] (www.cracs.aau.dk).

https://doi.org/10.1016/j.engfracmech.2024.110337
Received 23 March 2024; Received in revised form 8 July 2024; Accepted 26 July 2024
Available online 2 August 2024

Nomenclature

a, a_{tip}	Crack growth, position of the crack tip
C, C_I, C_{II}, C_m	Paris' law parameter, for mode I, mode II and mixed mode
cos_I, cos_{II}	Mode I and mode II direction cosines
D_k, D_e, D_i	Stiffness damage variable, energy damage variable, initiation damage variable
E_{11}, E_{22}, E_{33}	Longitudinal and transverse Young's moduli
G_c, G_{Ic}, G_{IIc}	Fracture toughness, mode I and mode II fracture toughnesses
G_I, G_{II}	Mode I and mode II energy release rates
G_{12}, G_{13}, G_{23}	Shear moduli
G_{max}	Maximum energy release rate during cyclic loading
J, J_I, J_{II}	J-integral, and mode I and mode II contributions
K	Penalty stiffness
l_i	Initiation length
L_j	Length of element j
m, m_I, m_{II}, m_m	Paris' law exponent, for mode I, mode II and mixed mode
N	Number of cycles
N_i	Number of cycles to initiation
s, s_I, s_{II}	Initiation S-N curve slope, for mode I and mode II
t, t_c	Time, current time
w_d, w_{tot}	Specific dissipated energy, total dissipated energy
w_k	Integration weight of integration point k
x_a	Coordinate along the interface in the growth driving direction
β	Displacement-based mode mixity
Δa_{target}	Target crack growth increment
ΔN, ΔN_p	Cycle increment, cycle increment defined by the propagation model
ΔN_i, $\Delta N_{i,region}$	Remaining number of cycles to initiation in a material point and in a crack initiation region
δ_0, δ_c	Onset and final equivalent displacements
δ_1, δ_2, δ_3	Separation components in shearing directions 1 and 2, and in opening direction 3
δ_I, δ_S, δ	Mode I and shear mode associated separations, mixed-mode equivalent displacement norm
η	B-K coefficient
ν_{12}, ν_{13}, ν_{23}	Poisson's ratios
ϕ	Energy-based mode mixity
τ, τ_{11}, τ_{33}	Traction, components in sliding direction 1 and opening direction 3
τ_0, τ_{I0}, τ_{II0}, τ_{S0}	Onset strength, and mode I, mode II and shear interface strengths
CZ, CZM	Cohesive Zone, Cohesive Zone Model
DCB	Double Cantilever Beam
DNS	Double Notched Shear
ENF	End-Notched Flexure
FEA	Finite Element Analysis
LEFM	Linear Elastic Fracture Mechanics
MMB	Mixed-Mode Bending
SBS	Short Beam Shear
UPF	User Programmable Feature
VCCT	Virtual Crack Closure Technique

Some researchers have proposed models where propagation is modelled as a succession of initiation occurrences [12–14]. In [12], Nojavan et al. model initiation as a reduction in the fracture toughness by lowering the cohesive strength while preserving the final displacement. The reduction of the fracture toughness is justified by previous experimental results where pristine specimens showed a lower fracture toughness after being subjected to high-cycle loading [15]. The model presented in [14] by Dávila was developed to initially rely solely on fatigue initiation data, though it was later modified to require only fatigue propagation data [16]. In both versions of the model, a heuristic expression is proposed for the evolution of the damage variable under fatigue loading. This model has been further developed and studied in recent works [16–22].

Other researchers have clearly differentiated between a cohesive element undergoing propagation or initiation, defining separate models. Most of these propagation models rely on Paris' law, which relates the crack growth rate to the energy release rate. One

example is the model proposed by Turon et al. in [23] as an extension of their static model from [24]. This model relies on calculating the length of the process zone, which is obtained analytically. Pirondi et al. in [25] also calculated the length of the process zone analytically. However, the energy release rate was based on the global strain energy output from the finite element analysis. Bak et al. in [26] circumvented the need to calculate the length of the fracture process zone by employing the J-integral along the cohesive region to obtain the energy release rate. This approach was shown to provide excellent results in [27] compared to contemporary models. This propagation model was later expanded and generalised to 3D curved structures in [28,29] and recently extended with multiple delamination capabilities in [30] using a floating node strategy. Another propagation model based on Paris' law is the one developed by Harper and Hallett in [31] for explicit finite element analyses. This model uses a quasi-static analysis to obtain the length of the fracture process zone, avoiding the reliance on an analytical expression, but adding an extra step. In [32], the model from [31] was modified to prevent the dependence on obtaining the length of the fracture process zone by restricting the fatigue damage calculation to the element at the crack tip. This model was employed with some modifications in [33–36]. This propagation model was extended to model also initiation in [37,38], where experimental data from an initiation S-N curve was employed to detect initiation, after which the traction of the 'initiated' element is reduced to zero. In [39], Iarve et al. proposed an initiation model where the cohesive law of the 'initiated' element is modified by reducing the interface strength to the traction at initiation and increasing the final displacement to keep the fracture toughness constant. This way, the mesh size dependency to be expected in a sudden degradation approach is avoided. . The modification to the cohesive law presented in [39] does not achieve the same instantaneous energy loss at initiation as obtained in [12], where the remaining ability to do non-conservative work is also lowered by reducing the fracture toughness. Additionally, cohesive elements subjected to initiation will reach full degradation for larger displacement jumps than cohesive elements undergoing pure propagation. The concept behind this initiation model was combined with the propagation model first presented in [31] in recent works [33,34,36].

The main purpose of the work presented in this paper is to add initiation capabilities to one of the most advanced and accurate delamination fatigue propagation models, presented in [26–30]. However, extending this model with existing fatigue initiation models, e.g. by the models of [12,16,39], is not straightforward. This is because the propagation model relies on the definition of a contour J-integral, which requires a well-defined crack tip. This need for a well-defined crack tip is also present in the Virtual Crack Closure Technique (VCCT), which is based on Linear Elastic Fracture Mechanics (LEFM). Nevertheless, it must be noted that, unlike VCCT, the proposed Cohesive Zone Model (CZM) can capture the development of the fracture process zone ahead of the crack tip, which may greatly impact the compliance of the specimen/structure being modelled [40].

This paper presents a model for delamination fatigue initiation, which at initiation introduces a fully damaged region, similar to [38]. From this region, a J-integral contour can be defined. This fatigue initiation model, combined with the state-of-the-art cohesive model for multiple delamination fatigue propagation from [26,30], can thus cover the entire span of delamination growth, from initiation to propagation. The fatigue initiation and propagation framework is implemented in ANSYS Mechanical APDL as a novel user cohesive element. A new bookkeeping strategy is developed in auxiliary user subroutines to study multiple delamination cases using a commercial FEA code. The bookkeeping strategy facilitates efficient tracking of all delamination fronts and J-contours to evaluate their energy release rates. The implementation has been evaluated using fatigue propagation-dominated test cases from literature: Double Cantilever Beam (DCB), End-Notched Flexure (ENF), Mixed-Mode Bending (MMB), moment-loaded DCB, and DCB with multiple delaminations. The evolution of the crack growth rate can be accurately predicted for single and complex multiple delamination cases. The initiation of delaminations under fatigue loading can also be satisfactorily obtained in three different fatigue initiation-dominated test cases from literature: Double Notched Shear (DNS), Short Beam Shear (SBS), and Three-Point Bending on 90° laminates. The potential of modelling propagation after initiation is also showcased. The ANSYS user cohesive element, together with the test cases, are made publicly available through the open-access GitHub repository: https://github.com/CraCS-research-group/ANSYS-Fatigue-Cohesive-Element with the following DOI address: https://doi.org/10.5281/zenodo.10226907, enabling other researchers, as well as the industry, to take advantage and further improve state-of-the-art delamination tools for modelling fatigue initiation and propagation.

The paper is organised as follows: Section 2 describes the formulation of the quasi-static, fatigue propagation, and fatigue initiation cohesive zone models. Section 3 outlines the user-defined cohesive zone element's numerical implementation in ANSYS Mechanical APDL. Section 4 presents and discusses the results from the test cases using the new user element. Finally, the conclusions are included in Section 5.

2. Formulation of the cohesive zone models

This section describes the cohesive zone models implemented in a user element in ANSYS Mechanical APDL. First, the quasi-static model is described (Section 2.1), followed by the fatigue propagation (Section 2.2) and initiation (Section 2.3) models.

2.1. Quasi-static cohesive zone model

The quasi-static model proposed by Turon et al. in [24], and extended in [41], is adopted in this work. A summary of the model is provided below.

The cohesive model divides the separations, i.e., the difference in the displacements between the upper and lower crack surfaces at the interface, in a component associated with the normal opening direction, δ_3, and the components in the shearing directions, δ_1 and δ_2. Mode I and shear mode associated separations can then be defined:

$$\delta_I = \frac{1}{2}(\delta_3 + |\delta_3|) \tag{1}$$

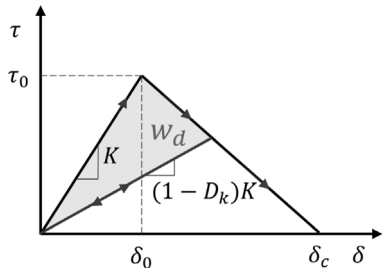

Fig. 1. Representation of a linear cohesive law. The shaded area represents the specific dissipated energy w_d.

$$\delta_S = \sqrt{\delta_1^2 + \delta_2^2} \tag{2}$$

A mixed-mode equivalent displacement norm δ is specified from the previous separations:

$$\delta = \sqrt{\delta_I^2 + \delta_S^2} \tag{3}$$

Fig. 1 represents the cohesive law, relating the traction τ to δ. Before onset, the constitutive behaviour follows a linear elastic relationship defined by a penalty stiffness K. Once δ exceeds its value at onset, δ_0, degradation of the interface takes place, controlled by the stiffness damage variable $D_k \in [0, 1]$. The area of the triangle delineated by the cohesive law is the fracture toughness G_c. The cohesive law is represented by the following equation:

$$\tau = (1 - D_k) K \delta \tag{4}$$

Interpenetration is avoided by employing an undamaged stiffness in the case of $\delta_3 < 0$. The onset and final equivalent displacements, δ_0 and δ_c, are calculated as follows:

$$\delta_0 = \frac{\tau_0}{K} \tag{5}$$

$$\delta_c = \frac{2G_c}{\delta_0 K} \tag{6}$$

The modified B-K criterion [24,42] is implemented to account for mixed-mode cases.

$$G_c = G_{Ic} + (G_{IIc} - G_{Ic}) B^\eta \tag{7}$$

$$\tau_0 = \sqrt{\tau_{I0}^2 + (\tau_{S0}^2 - \tau_{I0}^2) B^\eta} \tag{8}$$

$$B = \frac{\beta^2}{2\beta^2 - 2\beta + 1} \tag{9}$$

$$\beta = \frac{\delta_S}{\delta_I + \delta_S} \tag{10}$$

where τ_{I0} is the mode I interface strength, τ_{S0} is the shear interface strength, η is the B-K coefficient [42] used to model the variation of the fracture toughness with the mode mixity, K is the penalty stiffness before onset, G_{Ic} is the mode I fracture toughness, and G_{IIc} is the mode II fracture toughness. These six variables constitute the input data required by this quasi-static cohesive model.

Finally, the stiffness damage variable D_k is calculated using the following expression at any current time t_c. The irreversibility of the model is implemented such that D_k never decreases in value [41]:

$$D_k = min\left(max\left(0, \frac{\delta_c^t(\delta^t - \delta_0^t)}{\delta^t(\delta_c^t - \delta_0^t)}\right), 1 \right) \quad \forall \quad t \in [0, t_c] \tag{11}$$

For a more detailed explanation of the quasi-static cohesive model, the reader is referred to the work of Turon et al. in [24].

2.2. Fatigue propagation cohesive zone model

The delamination fatigue propagation model presented in [26–30] is used in the developed user cohesive zone element. A summary of the 2D model is provided below.

The fatigue propagation model follows the quasi-static cohesive law described in Section 2.1, but introduces a new damage variable D_e. D_e represents the fraction of the specific dissipated energy w_d to the fracture toughness G_c, as represented in Fig. 1. This energy damage variable relates to the previous stiffness damage variable D_k through the following expression:

$$D_e = \frac{w_d}{G_c} = 1 - \frac{K\delta_0\delta_c^2(1 - D_k)}{2G_c(\delta_c - D_k(\delta_c - \delta_0))} \tag{12}$$

The rate at which this new damage variable changes with the number of cycles at a specific point can be calculated from the global crack growth rate $\partial a/\partial N$ by differentiating the energy damage variable D_e with respect to the crack growth a:

$$\frac{\partial D_e}{\partial N} = \frac{\partial D_e}{\partial a}\frac{\partial a}{\partial N} \quad where \quad \frac{\partial D_e}{\partial a} = \left(F_\delta \frac{\partial \delta}{\partial a} + F_\beta \frac{\partial \beta}{\partial a}\right) \tag{13}$$

The derivative $\partial D_e/\partial a$ depends ultimately through the chain rule on the equivalent displacements, the mode mixity, the interface strengths and the derivatives with respect to the crack growth of the mixed-mode equivalent displacement norm $\partial\delta/\partial a$ and of the displacement-based mode mixity $\partial\beta/\partial a$. The expressions for these derivatives can be obtained from Eqs. (1), (2), (3), (10):

$$\frac{\partial \delta}{\partial a} = \begin{cases} \frac{\delta_I}{\delta}\frac{\partial \delta_3}{\partial a} + \frac{\delta_S}{\delta}\left|\frac{\partial \delta_1}{\partial a}\right| & \text{if } \delta_3 > 0 \\ \frac{\delta_S}{\delta}\left|\frac{\partial \delta_1}{\partial a}\right| & \text{if } \delta_3 < 0 \end{cases} \tag{14}$$

$$\frac{\partial \beta}{\partial a} = \begin{cases} \frac{\delta_I}{(\delta_S+\delta_I)^2}\left|\frac{\partial \delta_1}{\partial a}\right| + \frac{\delta_S}{(\delta_S+\delta_I)^2}\frac{\partial \delta_3}{\partial a} & \text{if } \delta_3 > 0 \\ 0 & \text{if } \delta_3 < 0 \end{cases} \tag{15}$$

Regarding the crack growth rate $\partial a/\partial N$, this propagation model is based on Paris' law, which relates $\partial a/\partial N$ to the energy release rate G. The Paris' law expression employed in this work uses the ratio between the maximum energy release rate during the cyclic loading G_{max} and the static critical energy release rate or fracture toughness G_c:

$$\frac{\partial a}{\partial N} = C\left(\frac{G_{max}}{G_c}\right)^m \tag{16}$$

The static critical energy release rate G_c is calculated at each instant in the analysis based on the energy-based mode mixity ϕ, i.e., the ratio of the energy release rates in mode I, G_I, and II, G_{II}. The sum of G_I and G_{II} is G_{max}.

$$G_c = G_{Ic} + (G_{IIc} - G_{Ic})\phi^\eta \tag{17}$$

$$\phi = \frac{G_{II}}{G_{II} + G_I} \tag{18}$$

The Paris' law parameters, C and m, are the input of this fatigue cohesive model. They must be obtained experimentally for modes I (C_I and m_I) and II (C_{II} and m_{II}), as well as for mixed mode (C_m and m_m). The effect of the mode mixity ϕ is accounted for as follows [43]:

$$C = \left(\frac{C_{II}}{C_I C_m}\right)^{\phi^2} C_m^\phi C_I \tag{19}$$

$$m = \phi^2(m_{II} - m_I - m_m) + \phi m_m + m_I \tag{20}$$

The calculation of the energy release rate components, G_I and G_{II}, is achieved by applying the J-integral contour to the cohesive zone. In [44], Rice first proposed using the J-integral in fracture problems to obtain the energy release rate associated with a particular crack tip. If the contour of this integral is chosen along the cohesive zone, the strain energy term is equal to zero. Therefore, the continuous expression of the J-integral J, and its mode I, J_I, and mode II, J_{II}, contributions, results in the following integration over the tractions and separations [26]:

$$J = J_I + J_{II} = -\int_{CZ} \tau_{33}\frac{\partial \delta_3}{\partial x_a}\, dx_a - \int_{CZ} \tau_{11}\frac{\partial \delta_1}{\partial x_a}\, dx_a \tag{21}$$

where τ_{33} and τ_{11} are the tractions in the opening direction 3 and the sliding direction 1, respectively, and x_a is the coordinate along the interface in the growth driving direction.

Finally, unlike in the static model, the complete degradation does not necessarily occur at δ_c. The reason is that an energy criterion is introduced to ensure that the relation between the tractions and the separations follows the cohesive zone law from the quasi-static model. This criterion forces complete degradation, $D_k = 1$, when the total dissipated energy w_{tot} exceeds the energy release rate G_{max}. The total dissipated energy w_{tot} represents the covered area of the cohesive law at the damaged state δ^t in the analysis, as indicated in Fig. 2.

$$w_{tot} = -\int_0^{\delta^t} \tau\, d\delta \tag{22}$$

For a more detailed explanation of the cohesive fatigue propagation model, including the complete derivation of $\partial D_e/\partial a$, the reader is referred to [26]. For its generalisation to 3D curved structures, the reader is referred to the following works [28,29,40,45].

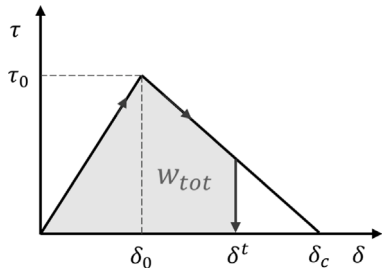

Fig. 2. Representation of the energy criterion for full degradation under fatigue loading.

2.3. Fatigue initiation cohesive zone model

The delamination fatigue propagation model described in Section 2.2 is combined with a fatigue initiation model to enable the simulation of initiation-dominated cases. These are cases where, before the cyclic load is applied, there is no well-defined crack tip, such as a pre-crack or elements fully damaged. The propagation model described before requires the existence of a crack tip for the J-integral contour to be well-defined, as described by Rice in [44]. Thus, the initiation model should allow discrete crack tips to originate in order to be compatible with the propagation model.

In the proposed fatigue initiation model, initiation is defined based on experimentally obtained initiation S-N curves. In this work, the S-N curve is defined as a plot between the maximum applied stress normalised with the static strength and the number of cycles to initiation N_i. The number of cycles to initiation N_i is calculated as follows:

$$N_i = 10^{\frac{1-\tau/\tau_0}{s}} \tag{23}$$

where τ is the current traction, τ_0 is the interface strength, and s is the slope of the S-N curve.

Similar to May and Hallett in [38] and in the spirit of the Palmgren-Miner's rule, a separate damage initiation variable D_i is introduced to identify how likely crack initiation is to occur at a specific material point. D_i is used as a status variable accounting for the accumulation of damage throughout the load history and does not modify the stiffness of the cohesive element. The value of D_i for a particular instant n is calculated based on its previous value at an instant $n-1$, the current cycle increment ΔN, and the number of cycles to initiation N_i [34]:

$$D_i^n = D_i^{n-1} + \frac{\Delta N}{N_i} \tag{24}$$

The remaining number of cycles to initiation for a material point is calculated as:

$$\Delta N_i = (1 - D_i) N_i \tag{25}$$

assuming that the internal and external load conditions remain constant.

To avoid mesh size dependencies, initiation is defined over a so-called crack initiation region rather than at a single material point. The crack initiation regions are defined from initiation points, i.e., material points with the local minimum ΔN_i, as marked in Fig. 3 with a cross. The crack initiation region comprises the neighbouring points, summing them up until the sum of their lengths reaches a predefined initiation length l_i, similar to the length of the initiation zone conceptually introduced in [38]. The value of l_i is part of the input of the cohesive zone model, along the interface properties, but this parameter is to be considered dependent on the interface and loading case, and likely as well on the laminate configuration. The crack initiation region is interpreted as the size and location of a detectable crack in the experiments used to characterise the S-N curve. In this way, l_i is the length of a detectable crack. Since different types of initiation experiments have different criteria for detecting crack initiation, this length will also depend on the given experimental set-up. Furthermore, knowing the exact size of l_i can be challenging as some initiation experiments have initiation based on a reduction of compliance, with no measurement of the initiated crack length, while others have concurrent initiation and final failure. Future research with dedicated crack initiation experiments where the length of the initiated crack is recorded is needed to validate this interpretation.

Once the crack initiation region has been identified, the remaining number of cycles to initiation associated with this region $\Delta N_{i,region}$ is calculated as the mean along its length l_i, as indicated in Eq. (26). This is done to limit the mesh size dependency that would originate when using the ΔN_i calculated at single points.

$$\Delta N_{i,region} = \frac{1}{l_i} \int_{l_i} \Delta N_i dx = \frac{1}{l_i} \int_{l_i} (1 - D_i) N_i dx \tag{26}$$

Initiation occurs when the remaining number of cycles to initiation in the crack initiation region $\Delta N_{i,region}$ becomes zero. The initiation criterion can thus be defined as:

$$\Delta N_{i,region} = 0 \tag{27}$$

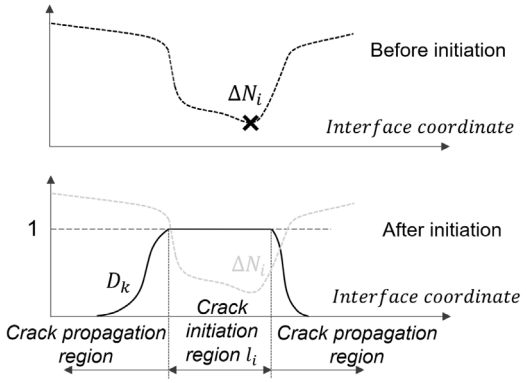

(a) Crack initiation region not centred around the point with the lowest value of ΔN_i.

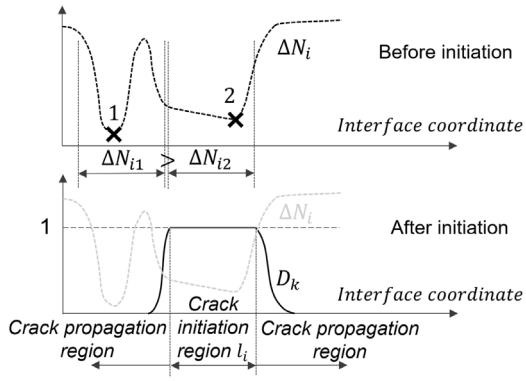

(b) Final crack initiation region based on the potential region with the lowest $\Delta N_{i,region}$.

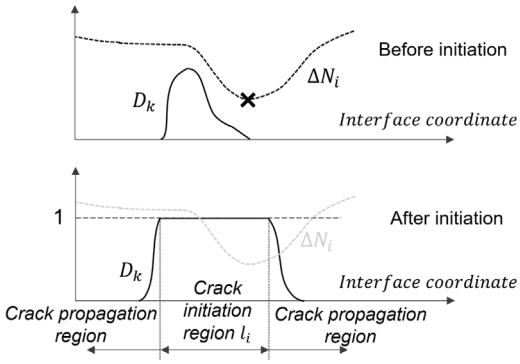

(c) Crack initiation region with statically damaged points.

Fig. 3. Creation of crack initiation and propagation regions along an interface in three different cases. Above: distribution of the remaining number of cycles to initiation ΔN_i before initiation occurs. Below: distribution of the stiffness damage variable D_k right after initiation.

When the initiation criterion is met, the proposed fatigue initiation model introduces a well-defined crack tip by enforcing full degradation, $D_k = 1$, to all material points in the crack initiation region. At the same time, the neighbouring points to this region can go through degradation following the quasi-static model described in Section 2.1. This degradation allows for the appearance of one or two so-called crack propagation regions extending beyond the edges of the crack initiation region. In this work, the term 'crack propagation region' refers to a region that ends on one side in at least one fully-damaged point or in a pre-crack modelled as a geometric discontinuity. The J-integral of such a crack propagation region can thus be calculated. The crack propagation region's growth is simulated using the fatigue model described in Section 2.2.

The creation of the crack initiation regions, and the resulting crack propagation regions , takes place following certain principles. These principles are illustrated using three different cases in Fig. 3. Each subfigure shows above the distribution of the remaining number of cycles to initiation ΔN_i before initiation occurs and below the stiffness damage variable D_k distribution right after initiation. The corresponding crack initiation region and crack propagation regions are also shown.

- The crack initiation region is identified as a set of neighbouring points around an extreme value of ΔN_i and is successively expanded by adding the neighbouring points with the lowest value of ΔN_i. This is continued until the predefined initiation length l_i is reached. As a consequence, the crack initiation region is not necessarily centred around the initiation point, as illustrated in Fig. 3(a).
- The crack initiation region is identified from several local initiation points, initially resulting in multiple potential crack initiation regions. The crack initiation region where damage is ultimately initiated by enforcing full damage is the one with the lowest $\Delta N_{i,region}$ as it will be the first one to meet the initiation criterion. This approach implies that the material point with the global minimum ΔN_i is not necessarily in the selected crack initiation region. This is illustrated in Fig. 3(b).
- Neighbouring material points that have previously developed damage under quasi-static loading are added to the crack initiation region, no matter ΔN_i. This approach is followed since static induced damage will reduce the traction level and result in an apparent higher ΔN_i even though these material points are physically more prone to initiation due to the weakened interface. This is illustrated in Fig. 3(c).

The effect of the mode mixity on the initiation S-N curve is incorporated as described in [38]. The S-N slope is calculated based on its values for mode I, s_I, and II, s_{II}, and the direction cosines cos_I and cos_{II}:

$$s = s_I cos_I^2 + s_{II} cos_{II}^2 \tag{28}$$

$$cos_I = \frac{\delta_I}{\delta} \tag{29}$$

$$cos_{II} = \sqrt{1 - cos_I^2} \tag{30}$$

The developed user element subroutine incorporates the possibility of estimating the initiation curve slopes from Paris' law data. This estimation allows for a simpler experimental interface characterisation, only requiring propagation tests and avoiding thus the complexity of fatigue initiation experiments. This estimation is based on the work of Allegri [13]. Based on a semi-analytical model, it was claimed that, if the initiation curve is defined as described in Eq. (23) and the propagation curve as in Eq. (16), the initiation slope s is half the inverse of the propagation slope m:

$$s = \frac{1}{2m} \tag{31}$$

This relationship is shown to provide a reasonable estimate in [14,16]. Nevertheless, if the assumption is tested with the experimental initiation and propagation data reported in [33,39], the resulting error in estimating the mode I data is significant, greater than 100% in [39], although around just 5% in mode II. If the comparison is made with the data from [37], the estimation error is much greater in mode II than in mode I, more than 50%. However, it must be noted that a great scatter characterises initiation tests and that different results have been obtained for mode II-dominated initiation depending on the specimen employed [46]. Furthermore, mechanisms such as plasticity may also explain why the relationship is not satisfied [16]. The estimation of the initiation data, according to Eq. (31), is carried out automatically by the user element subroutine if no initiation data is inputted.

3. Numerical implementation of the cohesive zone models in ANSYS

A novel combined implementation of the quasi-static model, the fatigue propagation model, and the fatigue initiation model, described in the previous section, is implemented as a User Programmable Feature (UPF) in ANSYS Mechanical APDL through the user-subroutine USERELEM. In addition, a new bookkeeping strategy allowing initiation and propagation modelling of multiple delaminations has been incorporated in the USERELEM.

A flowchart of the overall user element subroutine is provided in Fig. 4. This flowchart describes in general terms the various steps taken in each iteration to determine the cycle jump and calculate the damage state of the element. It is also identified whether the element is part of the pristine interface, a crack initiation region or a crack propagation region, and in the latter case computing the J-integral contribution of the element. Different actions are taken depending on whether this is the first element in a new iteration or a new substep, or whether it is a converged iteration. In ANSYS terminology, a converged iteration is an additional iteration after having reached converged equilibrium in the previous iteration. This iteration can be used to update those variables that are only to be calculated in a converged solution, such as the J-integral element contributions and the identification of the crack tip elements. The internal force vector and stiffness matrix must be provided as output of the subroutine in all iterations. Fig. 5 provides details on the calculation of the stiffness damage variable D_k for different cases using the quasi-static, fatigue propagation, or fatigue initiation models, respectively. The different steps and actions are described in more detail in the following subsections.

3.1. Element formulation

The fatigue propagation and initiation models' 2D formulation is implemented in a 3D element. The developed user-defined cohesive element is an 8-noded brick element with zero thickness. It uses a bi-linear interpolation of the separation between the lower and upper surfaces at the middle surface, where the natural coordinates are defined. The user can modify the number of integration points and the integration method, Newton–Cotes or Gauss, through the input provided to the element. This input, which includes the interface properties, is provided through the element's real constants.

3.2. Cycle-jump strategy

The user element subroutine applies a cycle-jump strategy [47]. In this approach, the first load step in the finite element analysis is a quasi-static ramp-up until the maximum applied load or displacement in the cyclic loading is achieved. The next load step in the analysis is where the fatigue loading is modelled. In this step, the maximum applied displacement or load is kept constant. The subroutine then advances the analysis by increasing the number of cycles with each substep. The subroutine calculates the effect that the increasing number of cycles has on the damage variables of the cohesive elements. The change in the damage variables, in turn, modifies the elements' stiffness and, thus, the response of the whole model as the delamination grows.

Regarding propagation, the cycle increment, ΔN_p, is obtained from the crack growth rate $\partial a/\partial N$, obtained from Eq. (16), and a target crack growth increment Δa_{target} provided by the user as input to the analysis. Furthermore, in the presence of multiple crack propagation regions, the minimum ΔN_p from all is chosen. This ensures that no crack propagation region advances more than the

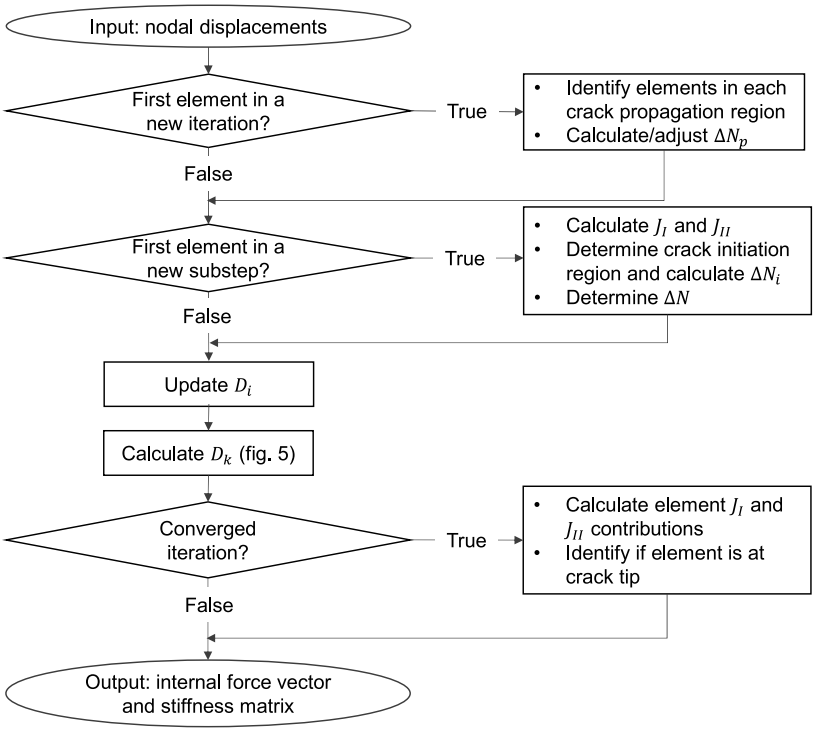

Fig. 4. Flowchart of the overall structure of the user cohesive element subroutine.

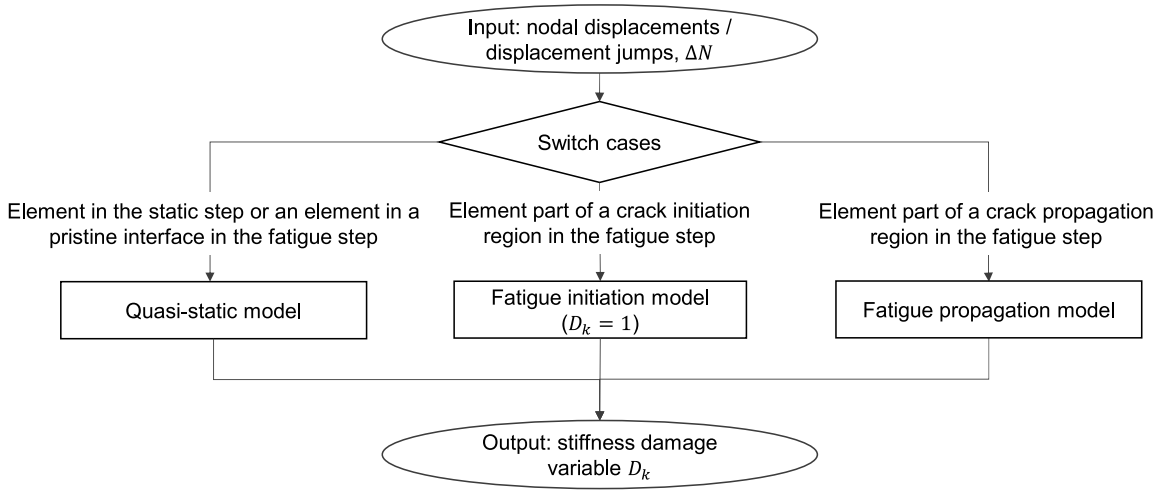

Fig. 5. Flowchart of the calculation of the stiffness damage D_k within the user cohesive element subroutine for three different cases.

defined target crack growth increment Δa_{target}, preventing convergence and accuracy issues. The calculation of ΔN_p is done at the beginning of each new iteration, as indicated in Fig. 4.

$$\Delta N_p = min\left(\frac{\Delta a_{target_m}}{(\frac{\partial a}{\partial N})_m}\right) \tag{32}$$

where m refers to the mth crack propagation region.

Regarding initiation, the cycle increment is defined as the minimum remaining number of cycles to initiation $\Delta N_{i,region}$ of all potential crack initiation regions: $\Delta N^{min}_{i,region}$. $\Delta N_{i,region}$ is calculated by discretising Eq. (26), as shown in Eq. (33). This is based on the approach by May and Hallett [38], computing $\Delta N_{i,region}$ as the average of the terms in the calculation of ΔN_i over the elements in a region consisting of n_{elem} elements:

$$\Delta N_{i,region} = max\left(\left(1-\overline{D_i}\right)10^{\frac{1-\overline{\chi_j}}{\overline{s_j}}},0\right) \tag{33}$$

$$\text{where} \quad \overline{D_i} = \frac{\sum_{j=1}^{n_{elem}} D_{i,j}}{n_{elem}}, \quad \overline{\chi_j} = \frac{\sum_{j=1}^{n_{elem}} \frac{\tau_j}{\tau_{0,j}}}{n_{elem}}, \quad \text{and} \quad \overline{s_j} = \frac{\sum_{j=1}^{n_{elem}} s_j}{n_{elem}}$$

where for each element j, τ_j is the current maximum element traction and $\tau_{0,j}$ is the cohesive strength. This calculation is done at the beginning of each new substep, as indicated in Fig. 4. Note that this calculation is only performed for elements that are initially part of the pristine interface. Only one crack initiation region can be introduced in each substep of the finite element analysis. Nevertheless, if there are two potential crack initiation regions with very similar remaining number of cycles to initiation $\Delta N_{i,region}$, the second crack initiation region may be introduced in the following substep after a small cycle increment ΔN. If $\overline{D_i}$ is greater than 1 in the second crack initiation region, following the introduction of the first crack initiation region, $\Delta N_{i,region}$ in this second region will result in zero cycles, see Eq. (33). A ΔN of zero cycles would result in both crack initiation regions being introduced in separate substeps in the numerical analysis but simultaneously in terms of the cycle count.

The cycle increment used in the cycle jump is selected as the lowest among the ones calculated for initiation and propagation:

$$\Delta N = min(\Delta N^{min}_{i,region}, \Delta N_p) \tag{34}$$

If initiation occurs because $\Delta N^{min}_{i,region} < \Delta N_p$, the crack initiation region and its corresponding crack propagation regions are introduced. If not, i.e., $\Delta N^{min}_{i,region} > \Delta N_p$, no crack initiation region is created. The resulting ΔN is used, whether initiation occurs or not, to propagate further any already existing crack propagation regions according to the fatigue propagation model.

3.3. Fatigue propagation model implementation

The implementation of the delamination fatigue propagation model in the user element subroutine is based on the automatic identification of any existing crack propagation regions. The energy release rate associated with each of the crack propagation regions is then calculated and used to obtain their respective crack growth rates $\partial a/\partial N$ using Eq. (16), and eventually the propagation-based cycle jump ΔN_p is determined using Eq. (32).

3.3.1. Automatic identification of multiple crack propagation regions

A new bookkeeping strategy is implemented to allow the modelling of multiple crack propagation regions under fatigue loading. This strategy starts by establishing a data structure with information about neighbouring cohesive elements based on the node numbering in the model. Fig. 6 shows the identification of the crack propagation regions for a specimen with two initial delaminations, modelled as free surfaces, from which three propagation regions are identified. Existing crack propagation regions are automatically identified in two steps:

- First, the crack tip elements are identified. Crack tip elements are defined as those elements which have an undamaged integration point on one side along the growth driving direction, while the integration point on the other side is partly or fully damaged [30]. This specification is checked for each element at the end of a converged substep in the analysis, as indicated in Fig. 4. A new crack propagation region is registered if the crack tip element is not already assigned to a specific crack propagation region. In Fig. 6, the crack tip elements, located at the edge of the region where $D_k > 0$, are marked with a cross.
- At the beginning of an iteration, the elements belonging to the crack propagation regions are identified, as shown in the flowchart in Fig. 4. For a newly registered crack propagation region, the neighbouring elements of the crack tip element, both those already damaged and those next in the growth driving direction, are assigned to the new crack propagation region. In case of an already registered crack propagation region, this crack propagation region is only extended further along the growth driving direction, since all the damaged elements are already included. This extension is performed to allow for further growth in the next substep within the definition of the crack propagation region. Fig. 6 shows how the crack propagation regions are defined from the elements at the crack tip, both in the region where $D_k > 0$ and in the growth driving direction.

3.3.2. J-integral calculation

The calculation of the J-integral provides both the total energy release rate and the mode mixity ϕ for each crack propagation region. In the implementation as a user cohesive element, the J-integral calculation from Eq. (21) is discretised and evaluated as a summation of the cohesive zone element contributions over the cohesive zone interface of each crack propagation region:

$$J = J_I + J_{II} = -\sum_{j=1}^{n_{elem}}\left[\frac{L_j}{2}\left(\frac{\partial\delta_3}{\partial x_a}\right)_j \sum_{k=1}^{n_{int\ points}} \tau_{33_k} w_k\right] - \sum_{j=1}^{n_{elem}}\left[\frac{L_j}{2}\left(\frac{\partial\delta_1}{\partial x_a}\right)_j \sum_{k=1}^{n_{int\ points}} \tau_{11_j} w_k\right] \tag{35}$$

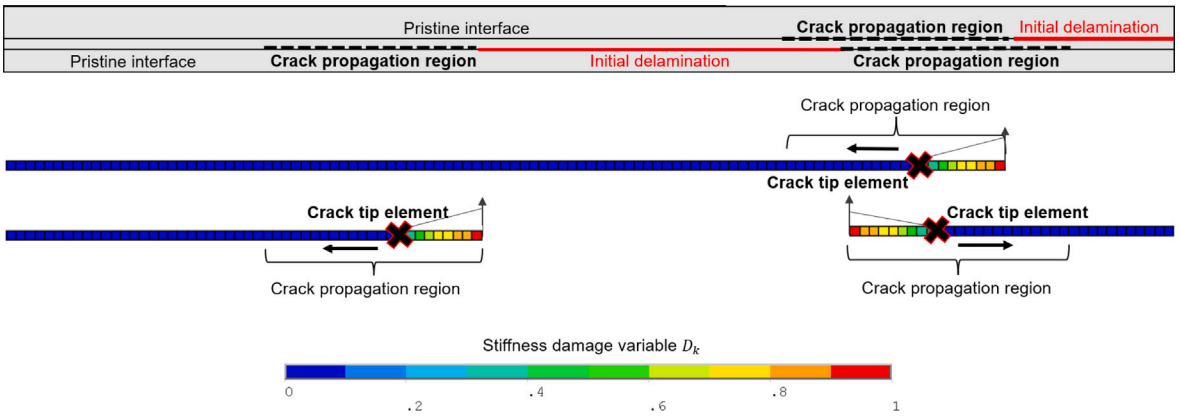

Fig. 6. Representation of the identification of three crack propagation regions in a specimen with two initial delaminations, modelled as free surfaces, in a side view of the specimen, and a plot of the stiffness damage variable D_k in the cohesive elements at both interfaces.

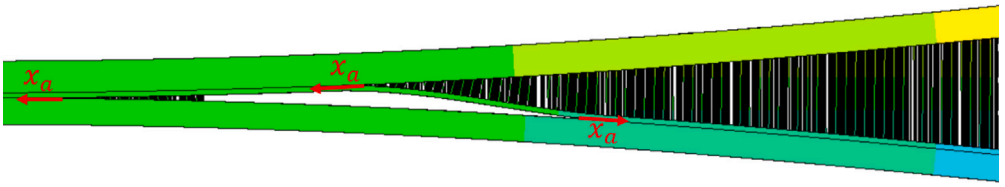

Fig. 7. Representation of the growth driving direction coordinate x_a, on the deformed finite elements results, for the three crack propagation regions present in this specimen.

where j refers to the jth element with $n_{int\ points}$ integration points, L_j is the element length, k refers to the kth integration point, τ_{33_j} and τ_{11_j} are the tractions at the integration points, and w_k is the integration weight. Note that this expression assumes linear cohesive elements. Furthermore, the J-integral evaluation assumes that the integration contours of multiple crack propagation regions within the same interface do not intersect.

The element contributions for the J-integral are calculated in the converged iteration of a substep. While the summation of element contributions to the J-integral of each crack propagation region is performed at the beginning of a new substep, as indicated in Fig. 4.

3.3.3. Determination of the growth driving direction

The growth driving direction, represented by coordinate x_a, is defined in the crack tip element according to integration point information, such that it is directed towards the direction of decreasing stiffness damage variable D_k [45], as shown in Fig. 7. The growth driving direction of each crack propagation region must be obtained, because it establishes the sign of the derivatives $\partial\delta_3/\partial x_a$ and $\partial\delta_1/\partial x_a$, included in the calculation of the J-integral in Eq. (35). Furthermore, the derivatives of the separations with respect to crack propagation, $\partial\delta_3/\partial a$ and $\partial\delta_1/\partial a$, which are used to obtain $\partial D_e/\partial N$ from Eqs. (13), (14), (15), are approximated as $-\partial\delta_3/\partial x_a$ and $-\partial\delta_1/\partial x_a$. This approximation assumes self-similar crack growth [26].

Since the elements are linear, i.e., they employ linear shape functions for the displacements, the derivatives $\partial\delta_3/\partial x_a$ and $\partial\delta_1/\partial x_a$ in the jth element can easily be determined by discrete differences:

$$\frac{\partial\delta_k}{\partial x_a} = \frac{\Delta\delta_k}{L_j} \tag{36}$$

The calculation of the derivatives based on the growth driving direction coordinate, x_a, is shown in Fig. 8.

4. Results and discussion

The results from various test cases are presented to showcase the different capabilities of the developed user cohesive element. The test cases are outlined in Tables 1 and 2. First, a specimen with multiple delaminations under quasi-static loading is presented in Section 4.1 to showcase the implementation of the quasi-static cohesive model in a complex case. Next, the implementation of the fatigue propagation model is considered in Section 4.2, both in standardised fracture toughness characterisation models and in a multiple delamination specimen. Finally, in Section 4.3, the fatigue initiation model and its combination with the propagation model are tested in three different test cases: Double Notched Shear (DNS) , Short Beam Shear (SBS), and Three-Point Bending on

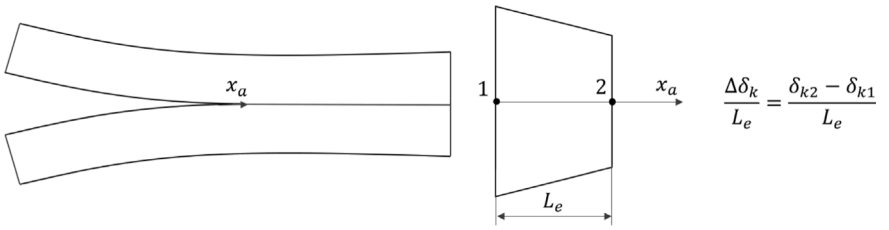

Fig. 8. Representation of the growth driving direction coordinate x_a and the calculation of the derivatives $\partial\delta_k/\partial x_a$ as discrete differences.

Table 1
Representations of the finite element models, and material and interface properties for the propagation-dominated test cases (Note that the dashed lines indicate MPCs and that plane-strain conditions, by restricting the out-of-plane displacement, are applied). Dimensions in mm.

Test case	Specimen	Material and interface properties	
Multiple delamination static [48,49]	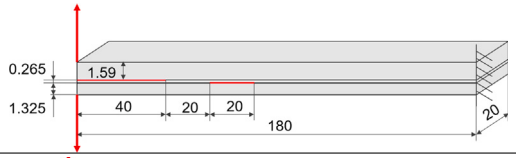	E_{11} = 115 GPa $G_{12} = G_{13}$ = 4.5 GPa $\nu_{12} = \nu_{13}$ = 0.29 G_{Ic} = 0.33 N/mm τ_{I0} = 33 MPa η = 2	$E_{22} = E_{33}$ = 8.5 GPa G_{23} = 3.48 GPa ν_{23} = 0.30 G_{IIc} = 0.80 N/mm τ_{II0} = 70 MPa K = 5.55 ·10^5 N/mm^3
Single delamination fatigue propagation [30]	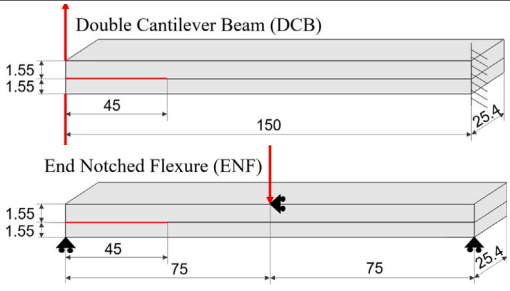	E_{11} = 120 GPa $G_{12} = G_{13}$ = 5.3 GPa $\nu_{12} = \nu_{13}$ = 0.30 G_{Ic} = 0.26 N/mm τ_{I0} = 30 MPa η = 2.73 C_I = 3.08 ·10^{-3} mm/cycle C_m = 458,087 mm/cycle m_{II} = 4.5	$E_{22} = E_{33}$ = 10.5 GPa G_{23} = 3.5 GPa ν_{23} = 0.51 G_{IIc} = 1.002 N/mm τ_{II0} = 60 MPa K = 30 ·10^5 N/mm^3 C_{II} = 1.49 ·10^{-1} mm/cycle m_I = 5.4 m_m = 4.94
Multiple delamination fatigue propagation [30]	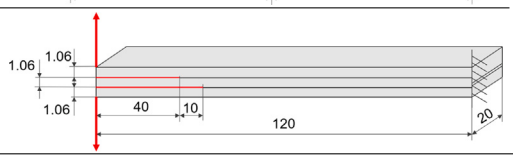		

90° laminates. Unlike the other test cases, there is no pre-crack in these last three cases, thus representing initiation-dominated cases.

Tables 1 and 2 include for each test case the representation of its finite element model, with its corresponding dimensions and boundary and loading conditions, as well as the material and interface properties. All the analyses were run using the commercial finite element software ANSYS Mechanical APDL, including the developed static and fatigue cohesive element implemented as user-defined programmable features (UPF). The specimens were all modelled using enhanced strain eight-noded SOLID185 elements. Despite using 3D solid elements, the finite element models are reduced to 2D by using one element through the width to match the 2D formulation of the fatigue initiation and propagation models. The user-defined cohesive elements employed 2x2 Newton–Cotes quadrature for the integration of the element stiffness matrix and the nodal force vector. The non-linear finite element analyses were solved using a standard Newton–Raphson scheme.

Besides the results shown in this paper, other study cases were run for the verification of the subroutine against analytical solutions: standardised fracture toughness characterisation models under static loading [24], and moment-loaded DCB specimens under fatigue loading [30].

Table 2
Representations of the finite element models, and material and interface properties for the initiation-dominated test cases (Note that plane-strain conditions, by restricting the out-of-plane displacement, are applied). Dimensions in mm.

Test case	Specimen	Material and interface properties	
Fatigue initiation [34,38,50]	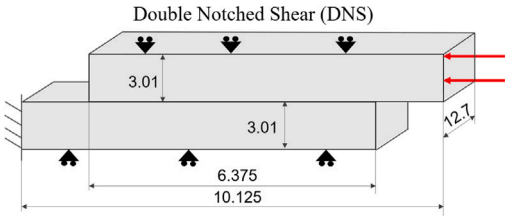	E_{11} = 161 GPa $G_{12} = G_{13}$ = 5.17 GPa $\nu_{12} = \nu_{13}$ = 0.325 G_{Ic} = 0.2 N/mm τ_{I0} = 60 MPa η = 2.73 C_I = 6.51 ·10^{-3} mm/cycle C_m = 458,087 mm/cycle m_{II} = 6.71 s_I = 0.072	$E_{22} = E_{33}$ = 11.4 GPa G_{23} = 3.98 GPa ν_{23} = 0.436 G_{IIc} = 1.0 N/mm τ_{II0} = 90 MPa K = 10^6 N/mm^3 C_{II} = 8.70 ·10^{-2} mm/cycle m_I = 5.29 m_m = 4.94 s_{II} = 0.12
	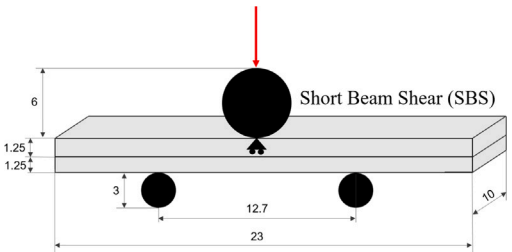	Same as above, except for: τ_{II0} = 95 MPa	s_{II} = 0.071
	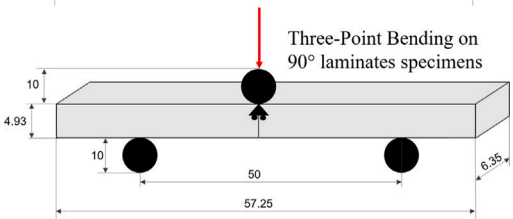	Same as above, except for: τ_{I0} = 92 MPa	

4.1. Static model with multiple delaminations

The capability of the developed cohesive element to model multiple delamination growth in complex cases was tested by simulating a modified Double Cantilever Beam (DCB) specimen with various delaminations growing under static loading.

This specimen was originally introduced and experimentally tested by Robinson et al. in [49], and it contains two initial delaminations in two different interfaces, as shown in the figure in Table 1. The element size along the length of the model is 0.1 mm, while the through-thickness element size is equal to the thickness of the middle layer, i.e. 0.265 mm. Furthermore, frictionless contact is used between the interfaces of the initial bottom delamination to avoid interpenetration between the middle and bottom layers. Displacements are applied as indicated in the figure in Table 1.

The specimen is made of Hexcel's HTA913 carbon fibre-reinforced epoxy prepreg. Its lay-up is $[0]_{24}$. The material properties of the specimen and the interfaces are the same as those employed by Russo and Chen in [48]. The properties are reported in Table 1.

The analysis is executed both under small and large displacement assumptions, controlled using the ANSYS APDL command 'NLGEOM'. The results are compared to the ones obtained by Russo and Chen in [48], who used linear and non-linear beam elements in a 1-mm mesh, as well as to the experimental results from Robinson et al. [49], in Fig. 9. It must be noted that it was necessary to introduce non-linear stabilisation through an energy-dissipation ratio to allow the analysis to converge after the snap-back at around 7 mm of opening displacement. The energy-dissipation ratio was set to a low value of 1E−6, which has been assessed to not affect the global response of the model.

The load–displacement curves obtained with the user-defined cohesive element match those from [48], even if the element size and type differ. The simulated load–displacement curves also follow the overall trend from the experimental results from [49]. These results show the capability of the current cohesive element implementation to model complex cases with multiple delaminations growing simultaneously.

4.2. Fatigue propagation

The developed cohesive element is now considered for the simulation of fatigue-driven delamination propagation. The modelling of fatigue propagation is shown in 4.2.1 for single delamination standardised fracture toughness characterisation tests: Double Cantilever Beam (DCB), End-Notched Flexure (ENF), and Mixed-Mode Bending (MMB). While in 4.2.2, the capability of modelling multiple delaminations under fatigue loading is evaluated in a modified DCB specimen. For all these test cases, the material and interface properties, reported in Table 1, are the same as those used in [30]. Furthermore, all cases were displacement-controlled.

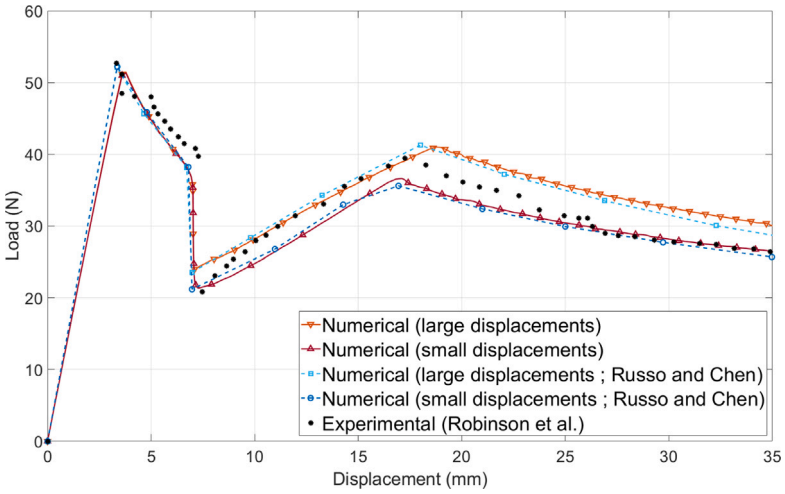

Fig. 9. Load–displacement curves for double-delamination DCB subjected to quasi-static loading. Comparison of the results obtained using the ANSYS user-defined cohesive element with the numerical results from [48] and the experimental ones from [49].

4.2.1. Single delamination fatigue cases

The geometry of each standardised fracture toughness characterisation specimen is described in Table 1. The lever length in the MMB model is calculated such that the mode mixity ϕ obtained in this analysis is 50%. In all the models, the crack is propagated 20 mm with a target crack growth increment Δa_{target} of 0.1 mm. The element size is set to 0.1 mm along the length of the specimens, while the through-thickness element size is 0.75 mm. Frictionless contact is used in the ENF model between the interfaces of the pre-crack to avoid interpenetration.

The results are shown in Fig. 10, plotting the crack growth rate $\partial a/\partial N$ against the maximum applied energy release rate G_{max}. The actual crack growth rate $\partial a/\partial N$ as it is realised in the simulation is obtained in each substep of the analysis by dividing the increment of the crack length by the cycle increment following a central difference. That is, for an instant n, $\partial a/\partial N_n = (a_{n+1} - a_{n-1})/(N_{n+1} - N_{n-1})$. The reason behind using a central difference is that in the implementation of a continuous cohesive zone model in a discrete finite element model, the calculated crack growth does not always match the length of the cohesive elements. If the crack does not propagate a discrete number of finite elements, $\partial a/\partial N_n$ varies sharply between substeps. A central difference decreases such variations. Note that the average crack growth rate over a few substeps is very close to the value evaluated using Paris' law. The numerical results are compared to the corresponding Paris' law, as described in Eq. (16).

It can be observed how the results obtained with the ANSYS user cohesive element match those obtained analytically. The small differences between the Paris' law and the numerical solutions originate from the numerical calculation of the crack growth rate, which is based on a finite difference approximation using discrete and simulated crack lengths.

4.2.2. Multiple delamination fatigue case

The implementation of the fatigue propagation model in the user-defined cohesive element is also evaluated in a modified DCB specimen with two initial delaminations at two different interfaces [30]. A representation of the specimen is shown in Table 1. The crack is propagated 10 mm with a target crack growth increment Δa_{target} of 0.1 mm. Along the length of the model, the element size is 0.1 mm. Three elements are used through the thickness of each arm to adequately capture the deformation of these arms, i.e., the mesh size through the thickness is around 0.35 mm.

In the multiple delamination fatigue case, propagation does not occur in pure mode I, as opposed to the single delamination fatigue case. Delamination propagation of the bottom interface occurs at a mode mixity ϕ of around 10%. The deformation of the middle arm induced by the bottom arm interface delamination leads to the delamination at the top interface propagating with a more significant sliding contribution, at approximately 42% of mode mixity ϕ. Compared to the single delamination cases, the interaction between both delaminations as they grow means that there is no available analytical solution which relates the crack length to the energy release rate, and thus to the number of cycles through Paris' law. Nevertheless, it is possible to obtain a 'semi-analytical' solution. The semi-analytical solution reads the number of cycles N and energy release rate values from the numerical results in each substep. The Paris' law expression is then used to obtain from the energy release rate the crack growth rate $\partial a/\partial N$. The position of the crack tip a_{tip} in an instant n is obtained by numerically integrating Eq. (16):

$$a_{tip_n} = a_{tip_{n-1}} + \frac{1}{2}\left(\left.\frac{\partial a}{\partial N}\right|_n + \left.\frac{\partial a}{\partial N}\right|_{n-1}\right)(N_n - N_{n-1}) \tag{37}$$

The evolution of the crack tip position is plotted against the number of cycles for each delamination in Fig. 11. As expected, the bottom interface delamination, referred to as bottom crack, which has a longer pre-crack, propagates faster. Comparing to the

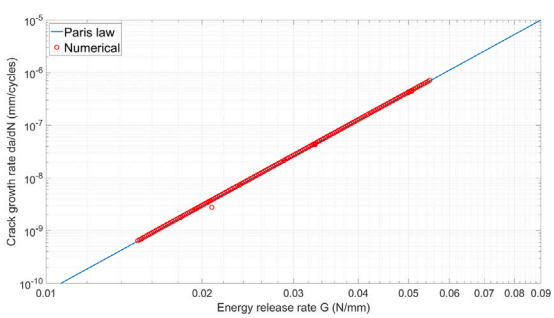

(a) DCB.

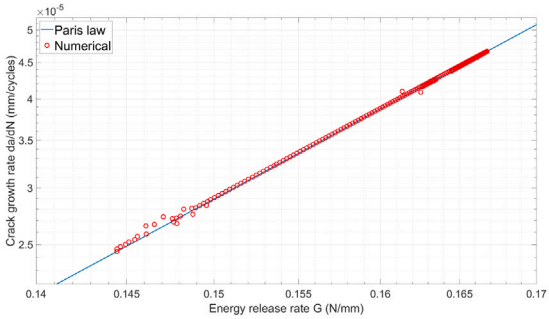

(b) ENF.

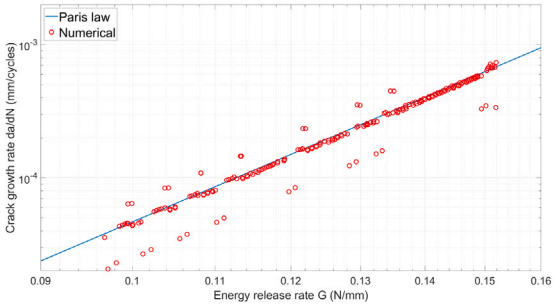

(c) MMB at mode mixity of 50%.

Fig. 10. Comparison of numerical results and Paris' law curves.

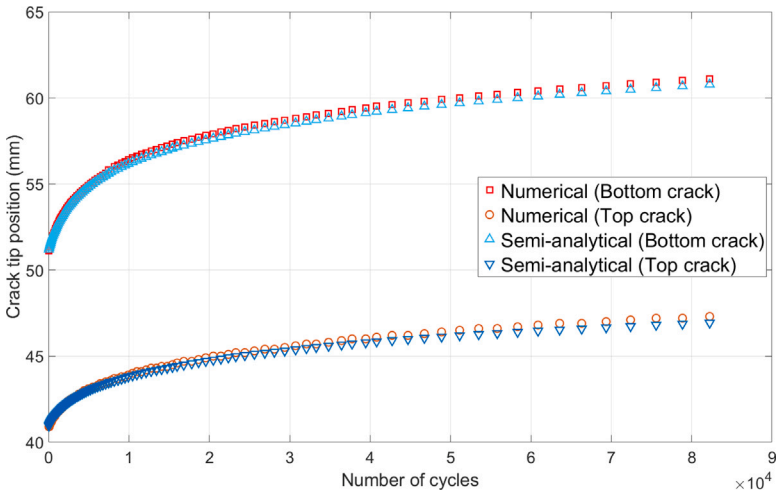

Fig. 11. Comparison of the numerical and semi-analytical crack tip position evolution vs number of cycles for the multiple delamination DCB specimen under fatigue loading, for the bottom and top cracks as represented in Table 1.

'semi-analytical' solution allows the verification of the numerical implementation of the cohesive model for multiple delaminations. A good match is obtained between the semi-analytical and numerical solutions. The differences between both solutions could again be explained by the fact that a continuous cohesive zone model is implemented in a discrete finite element model.

4.3. Fatigue initiation

The fatigue initiation model implemented in the user-defined cohesive element is evaluated in three different test cases: the mode II-dominated cases of Double Notched Shear (DNS) in 4.3.1 and Short Beam Shear (SBS) in 4.3.2, and the mode I-dominated Three-Point Bending on 90° laminates in 4.3.3.

4.3.1. Double Notched Shear

The fatigue initiation model is first assessed in the Double Notched Shear (DNS) specimen configuration considered by May and Hallett in [46]. These specimens were used to characterise initiation under shear loading. This type of loading is achieved by adding notches to a rectangular coupon tested under compression. Following the work of May and Hallett in [37], only a section of the DNS specimen is modelled. The resulting model can be seen in Table 2, where the geometry, dimensions, and boundary conditions are indicated. Along the length and thickness of the model, the element size is 0.05 mm. The target crack growth increment Δa_{target} used in the fatigue propagation model is 0.05 mm.

The DNS specimens tested in [46] were made of carbon fibre-reinforced epoxy prepreg IM7/8852. Their lay-up was $[0]_{24}$, with the material properties stated in Table 2. These properties were obtained from [30,34] with two exceptions. The slope of the initiation curve for mode II s_{II} from [38] is used instead, since it better corresponds to the experimental results reported in [46] for the DNS specimens. And the penalty stiffness K is set to 1x10^6 N/mm^3 based on a convergence analysis which assures constant results for the number of cycles to initiation.

In the experiments performed in [46], the DNS specimens were tested at different severities. The severity is defined here as the ratio between the applied shear stress and the static failure shear stress. The static failure stress was determined experimentally in [46] to be 82.5 MPa. The static failure stress obtained by the finite element model using the ANSYS user-defined cohesive element in a quasi-static simulation is 81.9 MPa, and thus almost exactly corresponds to the experimental one. In the fatigue simulations, the numerical model was subjected directly to loads, as indicated in the figure in Table 2, corresponding to the same severities as the specimens in the fatigue experiments: 30, 40, 50, 60 and 70%.

Determination of l_i

In the description of the delamination fatigue initiation model in Section 2.3, a parameter called the initiation length l_i is introduced. This parameter represents the length of the crack initiation region introduced in the model when initiation is predicted to occur. Generally, the lower this parameter l_i is, the greater the average of the initiation damage variable $\overline{D_i}$ will be, resulting in a lower remaining number of cycles to initiation $\Delta N_{i,region}$, as described in Eq. (33). The value of l_i could not be determined experimentally from current initiation tests. In some initiation tests, such as those conducted on the modelled DNS specimens, no initiation length could be measured because initiation coincides with specimen failure. In other tests, such as in the Short Beam Shear (SBS) specimens presented in [46], initiation is defined based on the change in the stiffness of the specimen, and there is no measurement of the length of the crack at the specific instants when initiation is established.. Based on previous literature, May and Hallett in [38] suggested a value for l_i between 0.3 and 3 mm, settling for 3 mm by fitting the numerical simulation to the experimental results.

In this work, similar to [38], l_i is thus selected to satisfy the behaviour observed experimentally: failure occurring right after initiation. That is, no stable propagation should take place after initiation has been detected. This requirement is satisfied for all severities if l_i is between 2.3 and 2.6 mm. In this range of values, a crack is first introduced in the model at the left notch in the figure in Table 2, followed by another crack in the right notch. The numerical analysis fails to converge in this second substep. Damping was introduced on the stiffness degrading damage variable D_k in the quasi-static damage model to delay the creation of the second crack. This allowed for convergence to take place, checking that indeed the stiffness damage variable D_k is equal or very close to 1 in all the cohesive elements in the second substep. This justifies thus equating non-convergence in the second substep of the numerical model to specimen failure.

Fatigue initiation results

Fig. 12 plots the number of cycles to initiation, which coincides with failure, against the experimental results, the fitted S-N curve used as input data in the model, and the numerical results obtained for some of the severities in [38]. The results obtained with the ANSYS user-defined cohesive element are plotted for the limits in the initiation length l_i range (2.3–2.6 mm) where the requirement of failure after initiation is satisfied.

A good alignment exists between the S-N curve and the results obtained with the user cohesive element. The numerical solutions provide a comparable slope to the one used as input. The results for l_i = 2.3 mm are slightly more conservative. The difference between the simulated results is small when compared to the extensive scatter seen in the experimental results. These results showcase the capability of the implemented cohesive element to model delamination fatigue initiation based on a successful determination of the initiation length.

Numerical example of the modelling of propagation after initiation

The value of the initiation length l_i is chosen in 4.3 to replicate the experimental behaviour, where the propagation is unstable and leads to failure after initiation. Nevertheless, using an artificially low l_i value, it is possible to demonstrate the capability of the user cohesive element to simulate propagation after initiation in a multiple delamination fatigue case. This capability is showcased in Fig. 13 for an l_i of 1 mm and a severity of 50%. This figure plots the stiffness damage variable D_k along the interface for different stages of the analysis. As explained in Section 2.1, D_k ranges from 0, before the onset of degradation, to 1, where the element is fully damaged.

- Fig. 13a shows the interface at the end of the static ramp-up in the cycle jump strategy. The stress concentrations at the notches lead to the cohesive elements in these regions starting to degrade without completely failing, i.e., $0 < D_k < 1$.

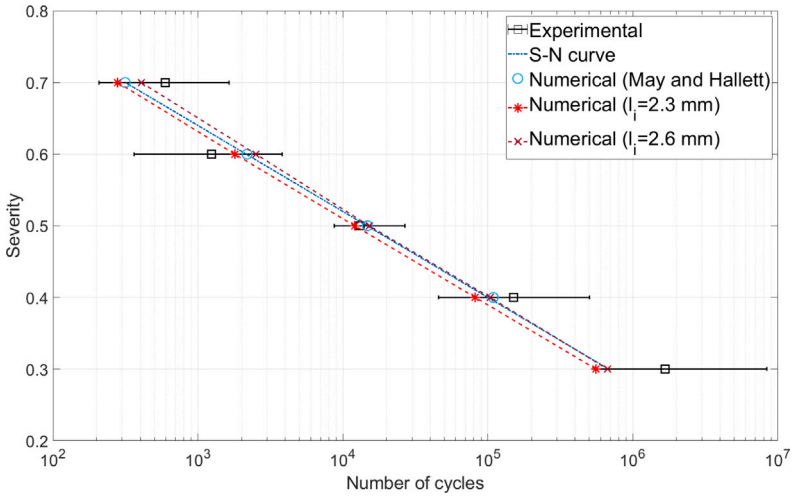

Fig. 12. Number of cycles to initiation/failure for DNS specimen at different severities. Comparison of the results obtained using the ANSYS user-defined cohesive element with the numerical results from [38] and the experimental ones from [46].

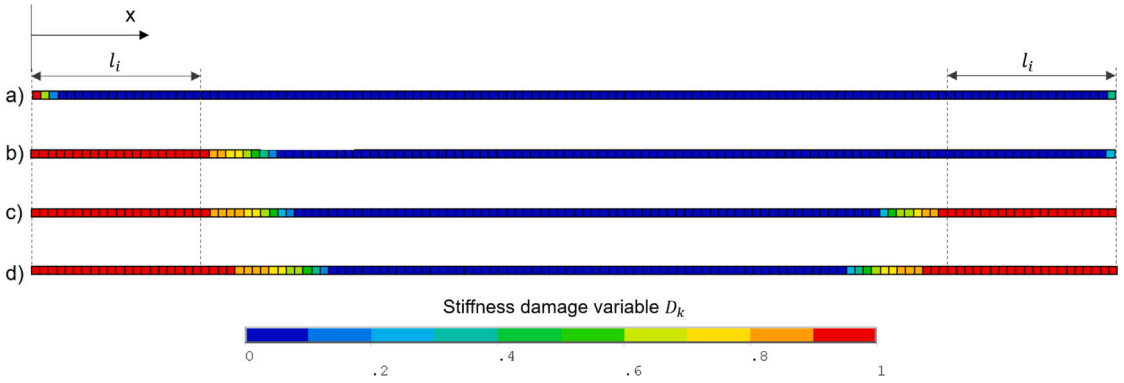

Fig. 13. Evolution of the stiffness damage variable D_k in the interface of a DNS specimen with an artificially low l_i. (a) At the end of the static ramp-up, (b) First fatigue substep, (c) Second fatigue substep, (d) A few substeps after in the fatigue simulation.

- Fig. 13b shows the occurrence of initiation in the left notch in the first fatigue substep. The element with the lowest remaining number of cycles to initiation ΔN_i is the one at the crack tip and not at the notch because of the lower stress level in the statically-damaged element. Nevertheless, the crack initiation region introduced spans the neighbouring elements, including the statically-damaged ones at the notch. The elements in the crack initiation region are fully damaged, i.e., $D_K = 1$. To the right of this region, a crack propagation region is formed as those elements degrade in this substep following the quasi-static damage model.
- Fig. 13c shows the occurrence of initiation in the notch on the right in the second fatigue substep. This second crack initiation region is introduced shortly after the first one. This exemplifies the importance of accounting for the initiation damage accumulation in previous substeps via Eq. (24). This way, the damage accumulated in the elements on the right during the first fatigue substep is accounted for in the calculation of the new cycle increment. A new crack propagation region appears. The growth of the crack propagation region on the left side can also be observed.
- In Fig. 13d, some substeps afterwards, both cracks have propagated further. No more crack initiation regions have been introduced, because the cycle increment calculated for the propagation of the two existing crack propagation regions is lower than what is required to introduce another crack initiation region, i.e., $\Delta N^{min}_{i,region} > \Delta N_p$.

4.3.2. Short Beam Shear

The fatigue initiation model is assessed next in another mode II fatigue initiation-dominated test case: the Short Beam Shear (SBS) specimen configuration also considered by May and Hallett in [46]. These specimens were also used to characterise delamination initiation under shear loading. The SBS specimens are Three-Point Bending specimens with a shorter support span to facilitate

interlaminar failure under shear loading. The finite element model is shown in Table 2, where the geometry, dimensions, and boundary conditions are indicated. The element size is set to 0.05 mm along the length of the specimen, while the through-thickness element size is 0.15 mm. The target crack growth increment Δa_{target} used in the fatigue propagation model is 0.05 mm. The user-defined cohesive elements are introduced in the mid-thickness of the specimen along its length. The support and loading rollers are assigned very high stiffnesses. While the loading roller can move vertically, the support rollers are fixed. Frictionless contact is modelled between the roller and specimen surfaces.

The SBS specimens tested in [46] were made of carbon fibre-reinforced epoxy prepreg IM7/8852. Their lay-up was $[0]_{20}$, with the material properties stated in Table 2. Two modifications are made with respect to the interface properties used in the DNS model. First, the slope of the initiation curve for mode II s_{II} from [34] is used since it better corresponds to the experimental results reported in [46] for the SBS specimens. Using different s_{II} values for the DNS and SBS cases was also justified in [38]. Second, the mode II interface strength τ_{II0} is set such that the static failure stress in a quasi-static simulation better matches that of the experiments. It is important to set the static strength with high accuracy so that applying the experimental load level in the numerical analysis corresponds to a similar severity. The severity is defined as the ratio between the applied shear stress and the static failure shear stress. τ_{II0} is increased from 90 MPa in [34] to 95 MPa to raise the numerically predicted failure stress from 90.7 MPa to 104.6 MPa. The experimental static failure stress was 103.2 MPa. The DNS specimen is simulated in cyclic load control at the same severities as in the experiments performed in [46]: 60, 70, 80 and 90%.

Determination of l_i

The initiation length l_i used in the SBS simulation has been calibrated using the DNS simulation since both are mode II fatigue initiation cases. Nevertheless, differences still exist between both tests. These differences are clearly illustrated by the dissimilar values of the slope of the initiation curve s_{II} obtained experimentally in [46]: 0.12 in the DNS case and 0.071 in the SBS case. Furthermore, it was reported in [46] that the delamination did not initiate through the whole width of the specimens, which further points to differences in the delamination behaviour between the two cases.

Fatigue initiation results

In the experiments of the SBS specimens carried out in [46], initiation is detected between the loading roller and one of the support rollers. After initiation, there is stable propagation, such that failure and initiation do not coincide in time, unlike in the DNS tests. The delamination growth evolution in the numerical model is shown in Fig. 14. This figure shows the stiffness damage variable D_k along the interface of the SBS specimen for different stages of the analysis. The SBS specimen is modelled for a severity of 70% and using the most conservative value of the initiation length l_i of 2.3 mm as determined in the DNS modelling.

- Fig. 14a shows the interface at the end of the static ramp-up in the cycle jump strategy. Unlike the DNS case, there is no quasi-static damage in any of the elements. However, the traction field varies along the interface. Based on the ΔN_i distribution, a crack initiation region is introduced in the next substep.
- Fig. 14b shows the occurrence of initiation between the loading roller and the right support roller at 10,697 cycles. The elements in the crack initiation region are fully damaged, i.e., $D_K = 1$. Crack propagation regions are formed to the right and left of this region, .
- Fig. 14c shows the growth of the crack propagation regions, mostly towards the right side of the crack initiation region, at 10,834 cycles. As indicated by the cycle count, this growth takes place at such a high rate that this instant can almost be understood as simultaneous to initiation. The lack of friction in the numerical model likely leads to an overestimation of the crack growth rate, as observed in [12]. The 90% severity is the only severity for which failure is predicted to occur at initiation, and the crack growth shown in this subfigure does not occur.
- Fig. 14d shows the crack after it reaches one of the specimen's ends and starts growing towards the other end. It corresponds to 26,705,064 cycles. The crack propagation slows down considerably once the crack passes the region under the loading roller, as indicated by the cycle count.

Except for the severity of 90%, the SBS numerical model predicts failure for an extremely large number of cycles. Nevertheless, this numerical prediction of failure cannot be compared to the experimental results for multiple reasons. First, no distinction is made in [46] between reporting catastrophic failure or meeting a maximum displacement criterion. Second, the numerical model cannot reproduce the 3D nature of delamination growth seen experimentally, where the crack does not extend through the width at initiation, and multiple delaminations in other interfaces appear. Third, the comparison to the experimental results is not straightforward due to their great scatter, and even the initiation experimental results do not show a good alignment to the fitted initiation S-N curve, as observed in Fig. 15.

Even if the numerical prediction of failure cannot be compared to the experimental results, that is not the case for the prediction of initiation. Friction and the 3D nature of delamination growth do not play a role at initiation. Furthermore, the comparison at initiation is made directly to the fitted S-N curve used as input in the model. Fig. 15 plots the number of cycles to initiation against the experimental results, the fitted S-N curve, and the numerical results obtained for some of the severities in [38]. The results obtained with the ANSYS user-defined cohesive element are plotted for the most conservative value of the initiation length l_i of 2.3 mm determined in the DNS modelling.

The agreement between the S-N curve and the results obtained with the ANSYS user-defined cohesive element is not as good as in the previous DNS case shown in Fig. 12. This difference can be explained partly by the fact that the same initiation length l_i is used, even if, as mentioned before, there exist differences between both mode II fatigue initiation tests. Nevertheless, the difference

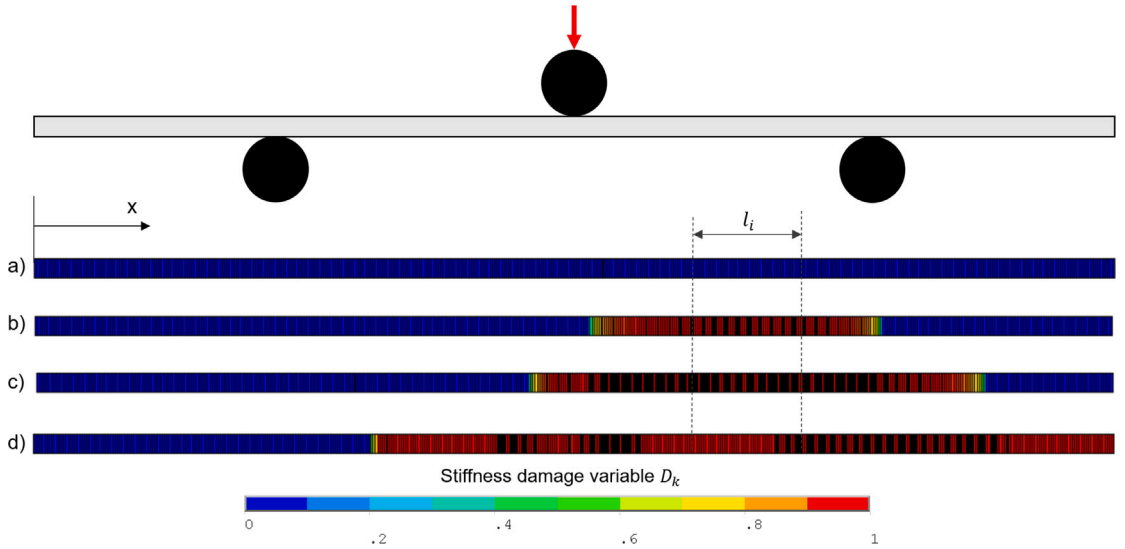

Fig. 14. Evolution of the stiffness damage variable D_k in the interface of a SBS specimen for a severity of 70% and l_i = 2.3 mm. (a) At the end of the static ramp-up (0 cycles), (b) First fatigue substep at 10,697 cycles, (c) Fatigue substep at 10,834 cycles, (d) Fatigue substep at 26,705,064 cycles.

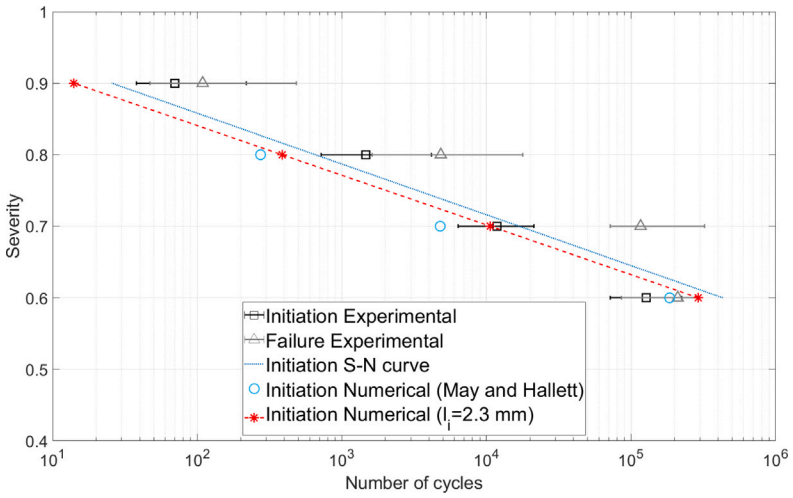

Fig. 15. Number of cycles to initiation and failure for SBS specimen at different severities. Comparison of the results obtained using the ANSYS user-defined cohesive element with the numerical results from [38] and the experimental ones from [46].

between the simulated results and the S-N curve is still smaller than the scatter seen in the experimental results. The numerical solutions provide a slope comparable to the one used as input and are also more conservative. These results showcase the capability of the implemented cohesive element to model delamination fatigue initiation based on the determination of the initiation length in an analogous test case.

4.3.3. Three-Point Bending on 90° laminates

The fatigue initiation model is considered next in a mode I fatigue initiation-dominated test case: the Three-Point Bending on 90° laminates investigated in [50]. Mode I failure takes place below the loading roller through the specimen's thickness. The finite element model is shown in Table 2, where the geometry, dimensions, and boundary conditions are presented. The element size is 0.5 mm along the length of the specimen, while the through-thickness element size is 0.05 mm. The target crack growth increment Δa_{target} used in the fatigue propagation model is 0.05 mm. The user-defined cohesive elements are introduced in the mid-span of the specimen along the thickness direction. The support and loading rollers are assigned very high stiffnesses. While the loading roller can move vertically, the support rollers are fixed. Frictionless contact is modelled between the rollers' and specimen's surfaces.

The specimens tested in [50] were made of carbon fibre-reinforced epoxy prepreg IM7/8852. Their lay-up was $[0]_{40}$, though the specimens were then cut and oriented in the test fixture at 90°. The material properties are stated in Table 2. Like the SBS model, the

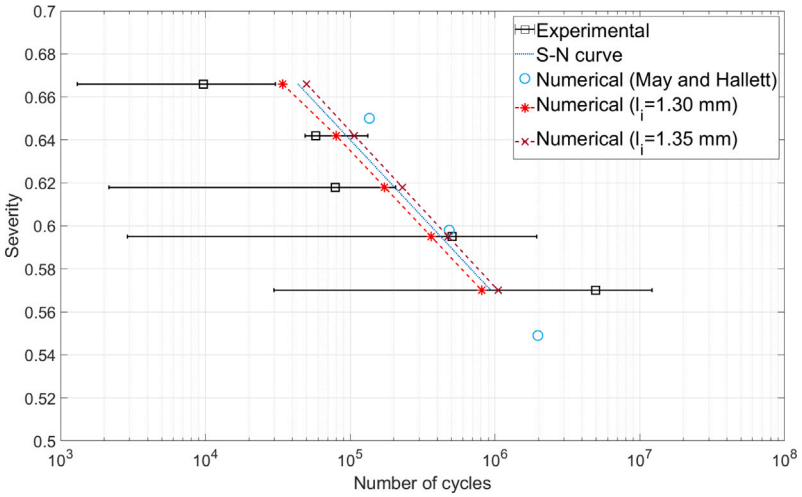

Fig. 16. Number of cycles to initiation/failure for Three-Point Bending on 90° laminates at different severities. Comparison of the results obtained using the ANSYS user-defined cohesive element with the numerical results from [37] and the experimental ones from [50].

mode I interface strength τ_{I0} is modified to better match the experimental static failure stress to the finite element model prediction in a quasi-static simulation. The severity is defined in this case as the ratio between the applied flexural stress and the static flexural failure stress. τ_{I0} is increased from 60 MPa in [34] to 92 MPa to raise the quasi-static prediction of the failure stress from 104.6 MPa to 127.9 MPa. The experimental static failure stress reported in [50] was 127.5 MPa. The specimen is simulated in cyclic load control at the same severities as in the experiments performed in [50]: 57.5, 59.5, 61.8, 64.2 and 66.6%.

Determination of l_i

Like the DNS tests, the Three-Point Bending on 90° laminates experience unstable propagation after initiation, such that failure and initiation coincide in time. In the DNS numerical models, the simultaneous occurrence of failure and initiation observed experimentally was replicated within a certain range of the initiation length l_i. Nevertheless, in the Three-Point Bending on 90° laminates, regardless of the l_i value, the numerical analysis always reaches non-convergence in the first substep of the fatigue analysis after introducing the crack initiation region. As in the DNS case, damping was introduced to check that non-convergence can be equated to specimen failure. It is concluded that the simultaneous occurrence of failure and initiation observed experimentally is replicated for all values of the initiation length l_i. Therefore, the initiation length l_i cannot be determined as in the DNS case. The approach chosen for the Three-Point Bending on 90° laminates is to obtain the values of l_i offering the best match between the experimental and numerical results for one of the tested severities, using then these values to model fatigue initiation in the remaining severities. For the lowest tested severity of 57%, this results in an l_i range between 1.30 and 1.35 mm.

Fatigue initiation results

Fig. 16 plots the number of cycles to initiation (and thus final failure) against the experimental results, the fitted S-N curve used as input data in the model, and the numerical results obtained for some of the severities in [37]. The results obtained with the ANSYS user-defined cohesive element are obtained for initiation lengths l_i of 1.30 and 1.35 mm in the fatigue initiation model.

A good agreement between the S-N curve and the results obtained with the user cohesive element is obtained for all severities besides the severity of 57% used to fit the initiation length parameter l_i. The difference between the simulated results is small compared to the extensive scatter in the experimental results. The numerical solutions provide a comparable slope to the one used as input. The numerical prediction for l_i=1.3 mm is slightly more conservative. These results showcase the capability of the implemented cohesive element to model delamination fatigue initiation for different load levels after calibrating the value of the initiation parameter l_i at one load level.

5. Conclusions

Damage modelling is crucial for the design of composite structures under fatigue loading, such as wind turbine blades with long service lives. For this purpose, a novel user-defined cohesive element has been implemented in commercial finite element software ANSYS Mechanical APDL. This cohesive element can be used to model fatigue-driven delamination initiation and propagation, which is a critical failure type in composite structures. A state-of-the-art propagation model has been combined with a new initiation model. The combination of both models allows for the simulation of the entire span of delamination failure, including initiation-dominated cases.

The state-of-the-art fatigue propagation model is based on Paris' law data and calculates the energy release rate through the J-integral. Its implementation on ANSYS is based on an efficient bookkeeping strategy, which allows the automatic tracking of the

multiple delaminations which may develop in the model. The fatigue initiation model uses initiation S-N data to determine the occurrence of initiation in a certain region of the model, the so-called crack initiation region, which is immediately fully damaged at initiation. In the edges of this region, so-called crack propagation regions, where a J-integral contour can be well-defined, are created, and the fatigue propagation model is applied in them. Each crack propagation region's growth driving direction and its respective energy release rate are calculated. The fatigue propagation and initiation models are combined in a cycle-jump strategy, which determines the cycle increment in each substep of the numerical analysis based on the occurrence of propagation or initiation.

The implementation of the quasi-static and fatigue propagation models in ANSYS through this new cohesive element has been validated in several test cases. First, a complex specimen with multiple delaminations was modelled under quasi-static loading. An excellent agreement is obtained in the load–displacement response compared to experimental and previously obtained numerical results. Second, the developed cohesive element was validated in single delamination fatigue propagation-dominated cases: Double Cantilever Beam (DCB), End-Notched Flexure (ENF), and Mixed-Mode Bending (MMB) specimens. The numerical results were compared to the corresponding Paris' law. Aside from the differences caused by the implementation of a continuous cohesive zone model in a discrete finite element model, the numerical results offered a strong match. Third, a modified DCB specimen with multiple delaminations was used to evaluate the capability of modelling multiple delaminations propagating under fatigue loading. The results for this multiple delamination specimen, where the position of the crack tip against the number of cycles is compared to a semi-analytical solution, also showed a good match.

In the fatigue initiation-dominated test cases, the implementation of the new fatigue initiation model and its combination with the fatigue propagation model were evaluated in three different specimens: Double Notched Shear (DNS), Short Beam Shear (SBS), and Three-Point Bending on 90° laminates. In the DNS case, the crack initiation region length parameter, l_i, was obtained by satisfying the condition imposed by the experimental behaviour: failure occurring right after initiation. Using the obtained l_i, the detection of initiation and the modelling of failure was successfully achieved in the DNS case, resulting in an excellent match to the experimental results. Furthermore, the DNS specimen was also employed to showcase the ability to model the initiation of multiple cracks and their successive propagation. The value of l_i calculated in the DNS case was used in the SBS test case, obtaining a good prediction of fatigue initiation despite the differences between these two mode II fatigue initiation cases. The SBS specimen also showcased the ability to model the successive propagation of multiple cracks from a crack initiation region. It must be noted that since it has yet to be investigated whether l_i can be regarded as an interface property, l_i must be considered a fitting parameter in this case. Finally, the Three-Point Bending on 90° laminates test case was used to study fatigue initiation under mode I. A good match was obtained between the experimental results and numerical prediction for all severities after fitting l_i with the results from one of the severities.

Finally, the ANSYS subroutine, whose development and evaluation in different test cases have been described in this paper, is made publicly available through the open-access GitHub repository: https://github.com/CraCS-research-group/ANSYS-Fatigue-Cohesive-Element with the following DOI address: https://doi.org/10.5281/zenodo.10226907. The ANSYS files of the test cases whose results have been shown in this paper are also made available. This will enable other researchers, as well as the industry, to make use and further improve state-of-the-art delamination tools for modelling fatigue growth.

CRediT authorship contribution statement

Iñigo Urcelay Oca: Writing – review & editing, Writing – original draft, Visualization, Validation, Software, Project administration, Methodology, Conceptualization. **Brian Lau Verndal Bak:** Writing – review & editing, Supervision, Software, Conceptualization. **Albert Turon:** Writing – review & editing, Software. **Esben Lindgaard:** Writing – review & editing, Supervision, Conceptualization.

Declaration of competing interest

The authors declare that they have no known competing financial interests or personal relationships that could have appeared to influence the work reported in this paper.

Data availability

The ANSYS user cohesive element, together with the test cases, are made publicly available through the GitHub repository: https://github.com/CraCS-research-group/ANSYS-Fatigue-Cohesive-Element.

Acknowledgements

This project has received funding from the European Union's Horizon 2020 Research and Innovation Programme (DyVirt – Dynamic Virtualization: modelling performance of engineering structures) under the Marie Skłodowska-Curie grant agreement No 764547, as well as from the Innovation Fund Denmark for the research project Affordable and Innovative Manufacturing of Large Composites (AIOLOS).

References

[1] Zuo Y, Montesano J, Singh CV. Assessing progressive failure in long wind turbine blades under quasi-static and cyclic loads. Renew Energy 2018;119:754–66. http://dx.doi.org/10.1016/j.renene.2017.10.103.

[2] Overgaard LC, Lund E. Structural collapse of a wind turbine blade. Part B: Progressive interlaminar failure models. Composites A 2010;41:271–83. http://dx.doi.org/10.1016/j.compositesa.2009.10.012.

[3] Ullah H, Alam K, Iqbal M, Husain A, Silberschmidt VV. Simulation of buckling-driven progressive damage in composite wind turbine blade under extreme wind loads. Eng Fail Anal 2022;140. http://dx.doi.org/10.1016/j.engfailanal.2022.106574.

[4] Wang Y, Soutis C. Fatigue behaviour of composite T-Joints in wind turbine blade applications. Appl Compos Mater 2017;24:461–75. http://dx.doi.org/10.1007/s10443-016-9537-9.

[5] Goutianos S, Sørensen BF. Fatigue crack growth rate at material and geometry transitions in glass-epoxy composites. Compos Struct 2021;275. http://dx.doi.org/10.1016/j.compstruct.2021.114445.

[6] Haselbach PU, Bitsche RD, Branner K. The effect of delaminations on local buckling in wind turbine blades. Renew Energy 2016;85:295–305. http://dx.doi.org/10.1016/j.renene.2015.06.053.

[7] Bender JJ, Hallett SR, Lindgaard E. Investigation of the effect of wrinkle features on wind turbine blade sub-structure strength. Compos Struct 2019;218:39–49. http://dx.doi.org/10.1016/j.compstruct.2019.03.026.

[8] Bender JJ, Hallett SR, Lindgaard E. Parametric study of the effect of wrinkle features on the strength of a tapered wind turbine blade sub-structure. Compos Struct 2019;218:120–9. http://dx.doi.org/10.1016/j.compstruct.2019.02.065.

[9] Chen X, Njomo-Wandji W, Miao XY. A robust and automated method for geometric modelling of thick laminates with multiple and asymmetric ply wrinkles. Compos Struct 2022;287. http://dx.doi.org/10.1016/j.compstruct.2022.115319.

[10] Cairns DS, Nelson JW, Woo K, Miller D. Progressive damage analysis and testing of composite laminates with fiber waves. Composites A 2016;90:51–61. http://dx.doi.org/10.1016/j.compositesa.2016.03.005.

[11] Mendonça HG, Mikkelsen LP, Zhang B, Allegri G, Hallett SR. Fatigue delaminations in composites for wind turbine blades with artificial wrinkle defects. Int J Fatigue 2023;175:107822. http://dx.doi.org/10.1016/j.ijfatigue.2023.107822.

[12] Nojavan S, Schesser D, Yang QD. An in situ fatigue-CZM for unified crack initiation and propagation in composites under cyclic loading. Compos Struct 2016;146:34–49. http://dx.doi.org/10.1016/j.compstruct.2016.02.060.

[13] Allegri G. A unified formulation for fatigue crack onset and growth via cohesive zone modelling. J Mech Phys Solids 2020;138. http://dx.doi.org/10.1016/j.jmps.2020.103900.

[14] Dávila CG. From S-N to the Paris law with a new mixed-mode cohesive fatigue model for delamination in composites. Theor Appl Fract Mech 2020;106. http://dx.doi.org/10.1016/j.tafmec.2020.102499.

[15] Ozturk A. The influence of cyclic fatigue damage on the fracture toughness of carbon-carbon composites. Composites A 1996;27:641–6. http://dx.doi.org/10.1016/1359-835X(96)00035-8.

[16] Dávila CG, Joosten MW. A cohesive fatigue model for composite delamination based on a new material characterization procedure for the Paris law. Eng Fract Mech 2023;284. http://dx.doi.org/10.1016/j.engfracmech.2023.109232.

[17] Liang YJ, Dávila CG, Iarve EV. A reduced-input cohesive zone model with regularized extended finite element method for fatigue analysis of laminated composites in abaqus. Compos Struct 2021;275. http://dx.doi.org/10.1016/j.compstruct.2021.114494.

[18] Joosten MW, Dávila CG, Yang Q. Predicting fatigue damage in composites subjected to general loading conditions. Composites A 2022;156. http://dx.doi.org/10.1016/j.compositesa.2022.106862.

[19] Raimondo A, Dávila CG, Bisagni C. Cohesive analysis of a 3D benchmark for delamination growth under quasi-static and fatigue loading conditions. Fatigue Fract Eng Mater Struct 2022;1–11. http://dx.doi.org/10.1111/ffe.13712.

[20] Leciñana I, Zurbitu J, Renart J, Turon A. A robust fatigue parameter determination method for a local fatigue cohesive zone model. Int J Fatigue 2023;171:107582. http://dx.doi.org/10.1016/j.ijfatigue.2023.107582.

[21] Leciñana I, Renart J, Turon A, Zurbitu J, Tijs BH. Characterization and analysis of the mode I interlaminar fatigue behaviour of thermoplastic composites considering R-curve effects. Eng Fract Mech 2023;286. http://dx.doi.org/10.1016/j.engfracmech.2023.109273.

[22] Hofman P, Meer FPVD, Sluys LJ. A numerical framework for simulating progressive failure in composite laminates under high-cycle fatigue loading. Eng Fract Mech 2024;295:109786. http://dx.doi.org/10.4121/20e3f4b.

[23] Turon A, Costa J, Camanho PP, Dávila CG. Simulation of delamination in composites under high-cycle fatigue. Composites A 2007;38:2270–82. http://dx.doi.org/10.1016/j.compositesa.2006.11.009.

[24] Turon A, Camanho PP, Costa J, Dávila CG. A damage model for the simulation of delamination in advanced composites under variable-mode loading. Mech Mater 2006;38:1072–89. http://dx.doi.org/10.1016/j.mechmat.2005.10.003.

[25] Pirondi A, Moroni F. A progressive damage model for the prediction of fatigue crack growth in bonded joints. J Adhes 2010;86:501–21. http://dx.doi.org/10.1080/00218464.2010.484305.

[26] Bak BLV, Turon A, Lindgaard E, Lund E. A simulation method for high-cycle fatigue-driven delamination using a cohesive zone model. Internat J Numer Methods Engrg 2016;106:163–91. http://dx.doi.org/10.1002/nme.5117.

[27] Bak BLV, Turon A, Lindgaard E, Lund E. A benchmark study of simulation methods for high-cycle fatigue-driven delamination based on cohesive zone models. Compos Struct 2017;164:198–206. http://dx.doi.org/10.1016/j.compstruct.2016.11.081.

[28] Carreras L, Turon A, Bak BLV, Lindgaard E, Renart J, de la Escalera FM, et al. A simulation method for fatigue-driven delamination in layered structures involving non-negligible fracture process zones and arbitrarily shaped crack fronts. Composites A 2019;122:107–19. http://dx.doi.org/10.1016/j.compositesa.2019.04.026.

[29] Carreras L, Bak BLV, Jensen S, Lequesne C, Xiong H, Lindgaard E. Benchmark test for mode I fatigue-driven delamination in GFRP composite laminates: Experimental results and simulation with the inter-laminar damage model implemented in SAMCEF. Composites B 2023;253:110529. http://dx.doi.org/10.1016/j.compositesb.2023.110529.

[30] Trabal GG, Bak BLV, Chen B, Carreras L, Lindgaard E. An adaptive floating node based formulation for the analysis of multiple delaminations under high cycle fatigue loading. Composites A 2022;160:107036. http://dx.doi.org/10.1016/j.compositesa.2022.107036.

[31] Harper PW, Hallett SR. A fatigue degradation law for cohesive interface elements - development and application to composite materials. Int J Fatigue 2010;32:1774–87. http://dx.doi.org/10.1016/j.ijfatigue.2010.04.006.

[32] Kawashita LF, Hallett SR. A crack tip tracking algorithm for cohesive interface element analysis of fatigue delamination propagation in composite materials. Int J Solids Struct 2012;49:2898–913. http://dx.doi.org/10.1016/j.ijsolstr.2012.03.034.

[33] Mukhopadhyay S, Nixon-Pearson OJ, Hallett SR. An experimental and numerical study on fatigue damage development in laminates containing embedded wrinkle defects. Int J Fatigue 2018;107:1–12. http://dx.doi.org/10.1016/j.ijfatigue.2017.10.008.

[34] Tao C, Mukhopadhyay S, Zhang B, Kawashita LF, Qiu J, Hallett SR. An improved delamination fatigue cohesive interface model for complex three-dimensional multi-interface cases. Composites A 2018;107:633–46. http://dx.doi.org/10.1016/j.compositesa.2018.02.008.

[35] Zhang B, Kawashita LF, Hallett SR. Composites fatigue delamination prediction using double load envelopes and twin cohesive models. Composites A 2020;129. http://dx.doi.org/10.1016/j.compositesa.2019.105711.

[36] Lu WT, Gao Z, Adluru HK, Hoos KH, Seneviratne WP, Mollenhauer DH, et al. Fatigue damage modeling in laminated composite by using Rx-FEM and strength tracking method. Composites A 2022;163. http://dx.doi.org/10.1016/j.compositesa.2022.107199.
[37] May M, Hallett SR. A combined model for initiation and propagation of damage under fatigue loading for cohesive interface elements. Composites A 2010;41:1787–96. http://dx.doi.org/10.1016/j.compositesa.2010.08.015.
[38] May M, Hallett SR. An advanced model for initiation and propagation of damage under fatigue loading - part I: Model formulation. Compos Struct 2011;93:2340–9. http://dx.doi.org/10.1016/j.compstruct.2011.03.022.
[39] Iarve EV, Hoos K, Braginsky M, Zhou E, Mollenhauer DH. Progressive failure simulation in laminated composites under fatigue loading by using discrete damage modeling. J Compos Mater 2017;51:2143–61. http://dx.doi.org/10.1177/0021998316681831.
[40] Carreras L, Lindgaard E, Renart J, Bak BLV, Turon A. An evaluation of mode-decomposed energy release rates for arbitrarily shaped delamination fronts using cohesive elements. Comput Methods Appl Mech Engrg 2019;347:218–37. http://dx.doi.org/10.1016/j.cma.2018.12.027.
[41] Lindgaard E, Bak BLV, Glud JA, Sjølund J, Christensen ET. A user programmed cohesive zone finite element for ANSYS mechanical. Eng Fract Mech 2017;180:229–39. http://dx.doi.org/10.1016/j.engfracmech.2017.05.026.
[42] Benzeggagh ML, Kenane M. Measurement of mixed-mode delamination fracture toughness of unidirectional glass/epoxy composites with mixed-mode bending apparatus. Compos Sci Technol 1996;56:439–49. http://dx.doi.org/10.1016/0266-3538(96)00005-X.
[43] Blanco N, Gamstedt EK, Asp LE, Costa J. Mixed-mode delamination growth in carbon-fibre composite laminates under cyclic loading. Int J Solids Struct 2004;41:4219–35. http://dx.doi.org/10.1016/j.ijsolstr.2004.02.040.
[44] Rice JR. A path independent integral and the approximate analysis of stress concentration by notches and cracks. J Appl Mech 1968;35:379–86. http://dx.doi.org/10.1115/1.3601206.
[45] Carreras L, Bak BLV, Turon A, Renart J, Lindgaard E. Point-wise evaluation of the growth driving direction for arbitrarily shaped delamination fronts using cohesive elements. Eur J Mech A Solids 2018;72:464–82. http://dx.doi.org/10.1016/j.euromechsol.2018.05.006.
[46] May M, Hallett SR. An assessment of through-thickness shear tests for initiation of fatigue failure. Composites A 2010;41:1570–8. http://dx.doi.org/10.1016/j.compositesa.2010.07.005.
[47] Paepegem WV. Developement and finite element implementation of a damage model for fatigue of fibre-reinforced polymers. Ghent University Architectural and Engineering Press; 2002.
[48] Russo R, Chen B. Overcoming the cohesive zone limit in composites delamination: Modeling with slender structural elements and higher-order adaptive integration. Internat J Numer Methods Engrg 2020;121:5511–45. http://dx.doi.org/10.1002/nme.6497.
[49] Robinson P, Besant T, Hitchings D. Delamination growth prediction using a finite element approach. Eur Struct Integr Soc 2000;27:135–47. http://dx.doi.org/10.1016/S1566-1369(00)80014-X.
[50] O'Brien TK, Chawan AD, Krueger R, Paris IL. Transverse tension fatigue life characterization through flexure testing of composite materials. Int J Fatigue 2002;24:127–45. http://dx.doi.org/10.1016/S0142-1123(01)00104-9.